1
Synthesis Mechanism: Crystal Growth and Nucleation

Pablo Cubillas and Michael W. Anderson

1.1
Introduction

Crystal growth pervades all aspects of solid-state materials chemistry and the industries that rely upon the functionality of these materials. In the drive toward greener, more efficient processes crystal engineering is an increasingly important requirement in materials such as catalysts; semiconductors; pharmaceuticals; gas-storage materials; opto-electronic crystals; and radio-active waste storage materials. In order to impart this desired functionality it is crucial to control properties such as crystal perfection, crystal size, habit, intergrowths, chirality, and synthesis cost [1].

The issues that concern crystal growth for nanoporous materials are similar to those that concern all crystal growths. Crystal habit and crystal size are of vital importance to the efficient functioning of these, and any other crystals, for real application. In the extreme case, single-crystal nanoporous films will require substantial skewing of both habit and size from normal bounds – this is currently impossible for zeolites but is being realized to some extent for metal organic framework (MOF) materials. Less extreme is the modification of crystal aspect ratio, for example, in hexagonal crystal systems where the pore architecture is often one-dimensional, growth of tablet-shaped crystals is usually preferred over more common needle-shaped crystals, particularly when molecular diffusion is important. All crystals incorporate both intrinsic and extrinsic defects, but whereas the presence of the latter may be easily controlled through purity of synthesis conditions, control of the former requires a deep knowledge of the underlying crystal growth mechanism. By defect we mean a well-defined aperiodic interruption in the periodic crystal structure. First, it is important to understand the nature of the defect, which normally requires a form of microscopy. Transmission electron microscopy (TEM) is the principal method used for this, but scanning probe microscopy is also useful. Owing to the structural complexity of framework crystals, each crystal system tends to display a unique defect structure that must be individually characterized. An extension of the same phenomenon is the incorporation of intergrowth and twin structures. Such defects are introduced during the crystal growth stage usually as a result of competing crystallization pathways that are near

Zeolites and Catalysis, Synthesis, Reactions and Applications. Vol. 1.
Edited by Jiří Čejka, Avelino Corma, and Stacey Zones

ISBN: 978-3-527-32514-6

energy equivalent. By understanding the growth mechanism it should be possible to identify the crucial step that controls this fork in the crystal growth, determine the energetic considerations, and predict modifications to growth conditions so as to enhance the probability of forming one particular crystal over another. This is crucial, for instance, for the preparation of chiral crystals that are assembled from a spiral stacking of achiral units [2, 3].

The advent of atomic force microscopy (AFM) (Figure 1.1) has opened up new possibilities to investigate the molecular events that occur during crystal growth and dissolution/recrystallization. The technique can be used both *in situ* and *ex situ* with each method suited to particular problems. *Ex situ* operation allows a vast array of synthetic parameters to be varied without concern for the delicacies of the AFM operation. In this respect, careful quenching experiments whereby the state of the nanoscopic features at the crystalline surface may be frozen rapidly before transfer to the AFM can be performed. This is crucial to prevent secondary processes caused by changing growth conditions upon crystal cooling and extraction from the mother-liquor. Rates and energies of crystal growth processes can be determined via such *ex situ* experiments through modeling both crystal topology and habit. *In situ* AFM gives a more direct approach to determining growth and dissolution rates. Further, surface structures that are inherently less stable may not be seen in *ex situ* analysis. Consequently, where possible, *in situ* analysis is preferred. The

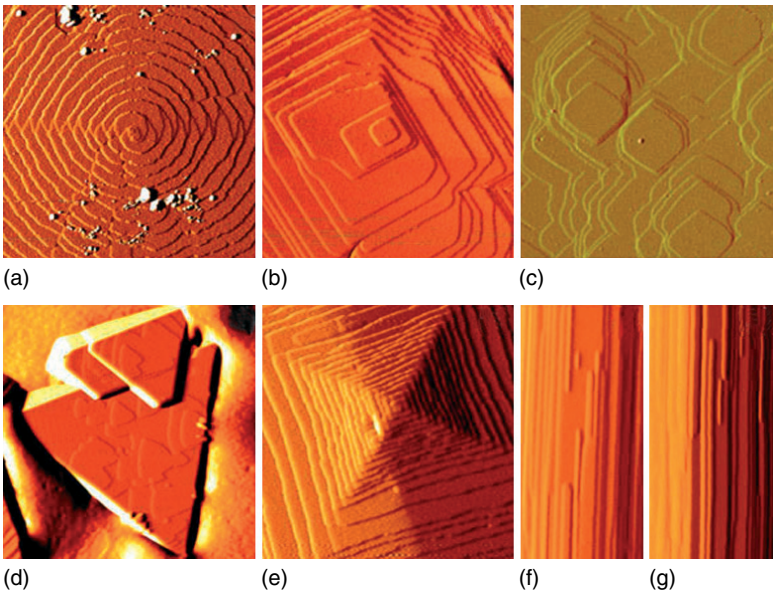

Figure 1.1 (a) Interlaced spiral on aluminophosphate STA-7; (b) zeolite A reducing supersaturation; (c) metal organic framework ZIF-8; (d) *in situ* $ZnPO_4$-FAU growth structure; (e) interlaced spiral $ZnPO_4$-SOD growth structure; and (f, g) *in situ* dissolution of zeolite L.

structural details leading to the observed crystal growth, defect, and intergrowth structure can also be probed using electron microscopy, and by slicing crystals open we can look at the consequences of structural growth decisions in the heart of the crystals. To probe the solution chemistry from which the crystals have evolved, a combination of the speciation delineation of nuclear magnetic resonance (NMR) with the speed and sensitivity of mass spectrometry is increasing our knowledge substantially. Both these techniques also probe the extent of oligomerization in the buildup to nucleation that can be further probed using cryo-TEM methods.

1.2 Theory of Nucleation and Growth

1.2.1 Nucleation

The formation of a new crystalline entity from a solution starts through the nucleation process. *Nucleation* is defined as the series of atomic or molecular processes by which the atoms or molecules of a reactant phase rearrange into a cluster of the product phase large enough as to have the ability to grow irreversibly to a macroscopically larger size. The *cluster* is defined as nucleus [4] or critical nuclei.

Nucleation can be homogeneous, in the absence of foreign particles or crystals in the solution, or heterogeneous, in the presence of foreign particles in the solution. Both types of nucleation are collectively known as *primary nucleation*. Secondary nucleation takes place when nucleation is induced by the presence of crystals of the same substance.

1.2.2 Supersaturation

The driving force needed for the nucleation and growth of a crystal is referred to as *supersaturation* and is defined as the difference in chemical potential between a molecule in solution and that in the bulk of the crystal phase:

$$\Delta\mu = \mu_s - \mu_c \tag{1.1}$$

where μ_s is the chemical potential of a molecule in solution and μ_c is the chemical potential of the molecule in the bulk crystal. Following thermodynamics Eq. (1.1) can be expressed as

$$\Delta\mu = kT \ln S \tag{1.2}$$

where k is the Boltzmann constant, T is the absolute temperature, and S is the supersaturation ratio. When $\Delta\mu > 0$ the solution is said to be supersaturated, meaning that nucleation and/or growth is possible, whereas when $\Delta\mu < 0$ the solution will be undersaturated and dissolution will take place. The form of

the supersaturation ratio will change depending on the system considered (i.e., gas/solid, solution/solid, melt/solid). For nucleation and growth from solutions it takes the following form:

$$S = \frac{\Pi a_i^{n_i}}{\Pi a_{i,e}^{n_i}} \tag{1.3}$$

where n_i is the number of ith ions in the molecule of the crystal, and a_i and $a_{i,e}$ the actual and equilibrium activities of the i molecule in the crystal.

1.2.3 Energetics

According to nucleation theory, the work necessary to form a cluster of n number of molecules is the difference between the free energy of the system in its final and initial states [4, 5] plus a term related to the formation of an interface between nucleus and solution. This can be expressed by (assuming a spherical nucleus):

$$\Delta G_T = -n\Delta\mu + 4\pi \cdot r^2\sigma \tag{1.4}$$

where r is the radius of the nucleus and σ is the surface free energy. If each molecule in the crystal occupies a volume V, then each nucleus will contain $(4/3)\pi \cdot r^3/V$ molecules. Eq. (1.4) will then take the following form:

$$\Delta G_T = -\frac{4}{3}\pi \cdot \frac{r^3}{V}\Delta\mu + 4\pi \cdot r^2\sigma \tag{1.5}$$

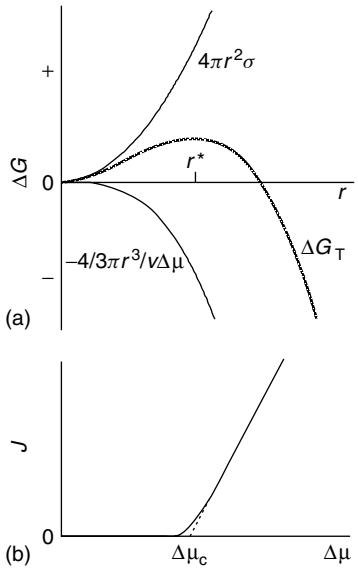

Figure 1.2 (a) Total free energy versus cluster size. (b) Nucleation rate as a function of supersaturation (showing the critical supersaturation).

Figure 1.2a shows a plot of ΔG_T as a function of r; it can be seen how the function reaches a maximum, which represents the energetic barrier that needs to be surpassed to achieve nucleation (ΔG^*). The *value of r at this maximum (r^*)* is defined as the critical radius or nucleus size [4, 5]. Its value is defined by

$$r^* = \frac{2\sigma \cdot V}{kT\ln S} \tag{1.6}$$

It has been proved that the value of r^* decreases (as well as that of ΔG^*) as the supersaturation increases [6], meaning that the probability of having nucleation in a given system will be higher, the higher the supersaturation.

1.2.4
Nucleation Rate

The rate of nucleation (i.e., the number of nuclei formed per unit time per unit volume) can be expressed by an Arrhenius-type equation [5]:

$$J = A \exp\left(\frac{-\Delta G^*}{kT}\right) \tag{1.7}$$

where A also depends on supersaturation. A typical plot of J as a function of supersaturation (S) is depicted in Figure 1.2b. It can be seen in this plot that the nucleation rate is virtually zero until a critical value of supersaturation is achieved, after which the rate increases exponentially. This critical supersaturation ($\Delta\mu_c$) defines the so-called metastable zone where crystal growth can proceed without concomitant nucleation taking place.

1.2.5
Heterogeneous and Secondary Nucleation

Equations (1.5) and (1.6) shows that both ΔG^* and r^* depend heavily on the surface free energy (σ), so any process that modifies this value will have an effect on the possible viability of the nucleation process. It has been proved that in the presence of a foreign substrate the decrease in the value of σ therefore reduces the values of ΔG^* and r^* at constant supersaturation [6], that is, making nucleation more favorable. A decrease in σ will also decrease the value of the critical supersaturation ($\Delta\mu_c$), since the nucleation rate is also dependent on the surface energy (Eq. (1.7)). This will make heterogeneous nucleation more viable than homogeneous nucleation at low supersaturation conditions. The reduction of the surface energy will be the highest when the best match between the substrate and the crystallizing substance is achieved. This situation is created, of course, when both the substrate and the crystallizing substance are the same, referred to as *secondary nucleation*. This mechanism will be more favorable than both heterogeneous and homogeneous nucleation and thus produced at lower supersaturation.

1.2.6
Induction Time

Induction time is defined as the amount of time elapsed between the achievement of a supersaturated solution and the observation of crystals. Its value will thus depend on the setting of $t = 0$ and the technique used to detect the formation of crystals. The induction period can be influenced by factors such as supersaturation, agitation, presence of impurities, viscosity, and so on. Mullin [5] defined the induction time as

$$t_i = t_r + t_n + t_g \tag{1.8}$$

The induction time is separated into three periods: t_r is the relaxation time, required for the systems to achieve a quasi-steady-state distribution of molecular clusters; t_n is the time required for the formation of a nucleus; and t_g is the time required for the nucleus to grow to a detectable size.

1.2.7
Crystal Growth

Crystal growth is the series of processes by which an atom or a molecule is incorporated into the surface of a crystal, causing an increase in size. These different processes can be summarized into four steps [7, 8] illustrated in Figure 1.3:

1) transport of atoms through solution;
2) attachment of atoms to the surface;
3) movement of atoms on the surface;
4) attachment of atoms to edges and kinks.

The first process is the so-called transport process, whereas 2–4 are referred to as *surface processes* (and may involve several substeps). Since these different steps normally occur in series, the slowest process will control the overall crystal growth. Therefore, growth can be transport (when step 1 is the slowest) or surface controlled (when steps 2–4 are the slowest).

1.2.8
Crystal Surface Structure

Crystal growth theories are based on considerations of the crystal surface structure. One of the most commonly used models was that provided by Kossel [9]. This model envisions the crystal surface as made of cubic units (Figure 1.4) which form layers of monoatomic height, limited by steps (or edges). These steps contain a number of kinks along their length. The area between steps is referred to as a *terrace*, and it may contain single adsorbed growth units, clusters, or vacancies. According to this model, growth units attached to the surface will form one bond, whereas those attached to the steps and kinks will form two and three bonds, respectively. Hence, kink sites will offer the most stable configuration. Growth will then proceed by

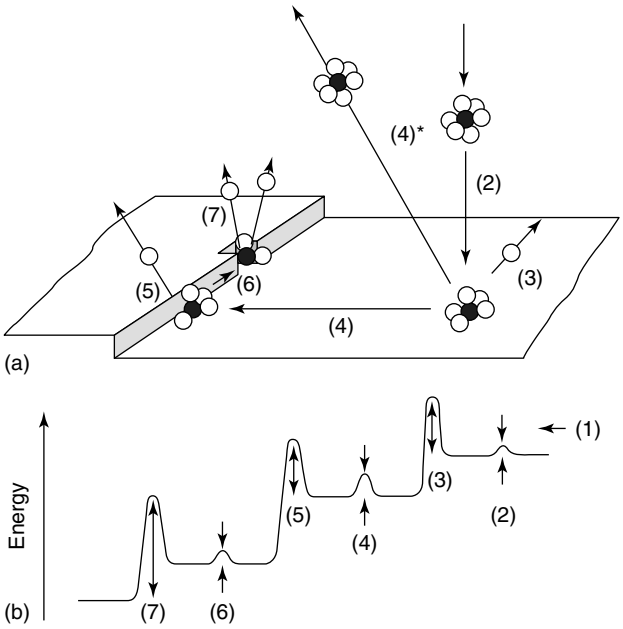

Figure 1.3 (a) Schematic representation of processes involved in the crystal growth: (1) Transport of solute to a position near the crystal surface; (2) diffusion through boundary layer; (3) adsorption onto crystal surface; (4) diffusion over the surface; (4*) desorption from the surface; (5) attachment to a step or edge; (6) diffusion along the step or edge; (7) Incorporation into kink site or step vacancy. (b) Associated energy changes for the processes depicted in (a). Figure modified from Elwell *et al*. [7].

the attachment of growth units to kink sites in steps. The kink will move along the step producing a net advancement of the step until this step reaches the face edge. Then, a new step will be formed by the nucleation of an island of monolayer height (or two-dimensional (2D) nucleus) on the crystal surface. This mechanism of growth is normally referred to as *layer growth* or *single nucleation growth* and is represented in Figure 1.5. A variation of this growth mechanism occurs when the nucleation rate is faster than the time required for the step to cover the whole crystal surface. In this case, 2D nuclei will form all over the surface and on top

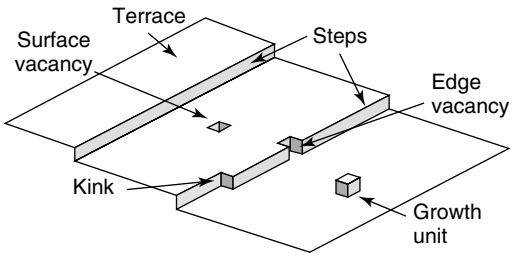

Figure 1.4 Kossel model of a crystal surface.

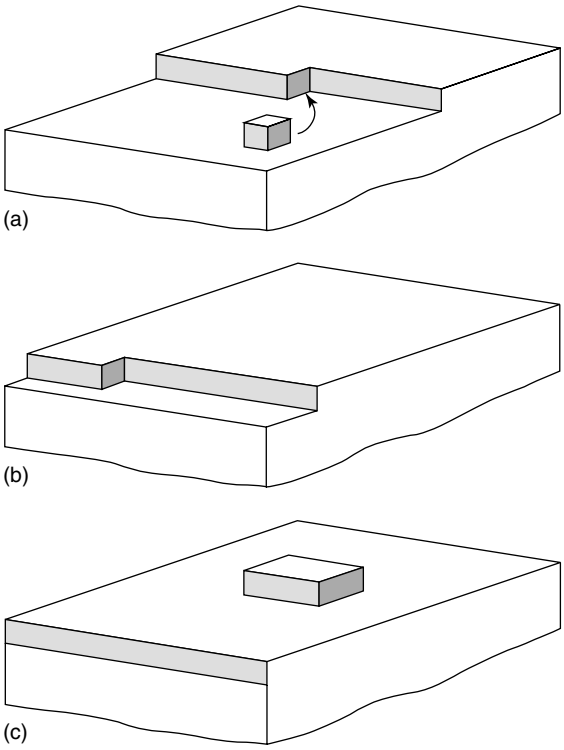

Figure 1.5 Schematic representation of layer growth. (a) Incorporation of growth units into step. (b) The step has almost advanced to the edge of the crystal. (c) Formation of 2D nucleus.

of other nuclei. These nuclei will spread and coalesce forming layers. This growth mechanism is normally referred to as *multinucleation multilayer growth* or *birth and spread* [10].

1.2.9
2D Nucleation Energetics

The total free energy change due to the formation of a 2D nucleus of height h and radius r can be calculated by using Eq. (1.5):

$$\Delta G_{T-2D} = -\pi \cdot \frac{hr^2}{V}\Delta\mu + 2\pi \cdot rh\sigma \tag{1.9}$$

The maximum of this function defines the value of the critical radius which is given by

$$r_{2D}{}^{*} = \frac{\sigma \cdot V}{kT \ln S} \tag{1.10}$$

It can be seen that the value of r_{2D}^* is half of the nucleus size for homogeneous nucleation (Eq. (1.6)).

1.2.10 Spiral Growth

The energetics of layer growth predict that growth takes place at relatively high supersaturation (needed to overcome the energy barrier associated with 2D nucleation). Nevertheless, it has been observed that crystals can still grow at lower supersaturation than predicted [11]. This dilemma was solved by Frank [12] who postulated that crystal surfaces are intercepted by dislocations. These dislocations will create steps in the surface, obviating the necessity for 2D nucleation. Figure 1.5 shows a schematic diagram on the formation and development of spiral growth. In the initial stage the dislocation creates a step (Figure 1.6a). Growth units attach to the step making it advance and thus generating a second step (Figure 1.6b). This second step will not advance until its length equals $2r_{2D}^*$; this is because any growth of a step with a smaller size is not thermodynamically favored. Once the second step starts advancing, it will generate a third step which in turn will not start moving until its length equals $2r_{2D}^*$ (Figure 1.6c), then a fourth step will appear, and so on (Figure 1.6d). This will generate a spiral pattern around the dislocation core, and a self-perpetuating source of steps where growth requires less energy than a layer mechanism (therefore, it can proceed at smaller supersaturation). In the case of a curved step, the spiral will be rounded and its curvature will be determined by the r_{2D}^* value at the specific supersaturation conditions in which

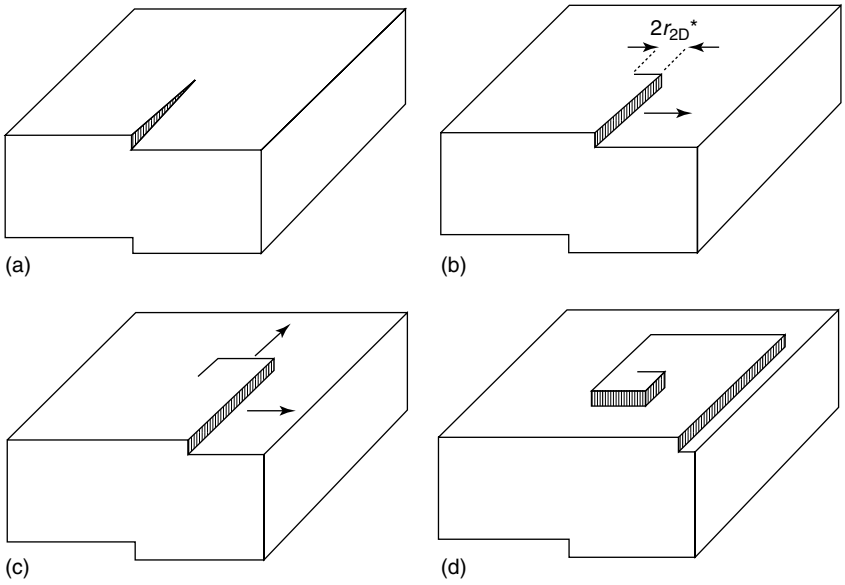

Figure 1.6 Development of a polygonal spiral.

the crystal grows. The theory of crystal growth by spiral dislocation was further refined by Burton, Cabrera, and Frank [13], giving rise to what is known as the *BCF theory*.

1.2.11
Interlaced Spirals

Interlaced spirals are the result of a periodic stacking of differently oriented growth layers, each having a different lateral anisotropy of step velocity [14]. In other words, in this type of spiral a step with unit cell may dissociate in substeps symmetrically related but crystallographically different. The dissociation is the result of a different growth anisotropy by each step due to its different crystallography. Figure 1.7 shows a schematic diagram showing the formation of a spiral of this type according to van Enckevort [14]. The surface in the figure is produced by two distinct types of steps (I and II), of height 1/2 d_{hkl}, emanating from a central point O. Layers of type I are bound by steps a and b, whereas layers from type II are bound by steps c and d. Steps a and d move fast and steps b and c move slowly. This results in steps a of layer I catching up with steps c from layer II, producing a double step of unit-cell height. The same process is observed in steps d joining the slow steps b. The result is a pattern of unit-cell height steps with interlaced crossovers formed by lower steps of height 1/2 d_{hkl}. Interlaced spirals have been observed in numerous systems, including barite [15], molecular crystals [16, 17], silicon carbide [18], GaN [19], and sheet silicates [20].

1.2.12
Growth Mechanisms: Rough and Smooth Surfaces

The growth mechanisms can be classified into three types depending on the interface structure. If the surface is rough the growth mechanism will be of adhesive type, whereas if the surface is smooth growth will take place by either

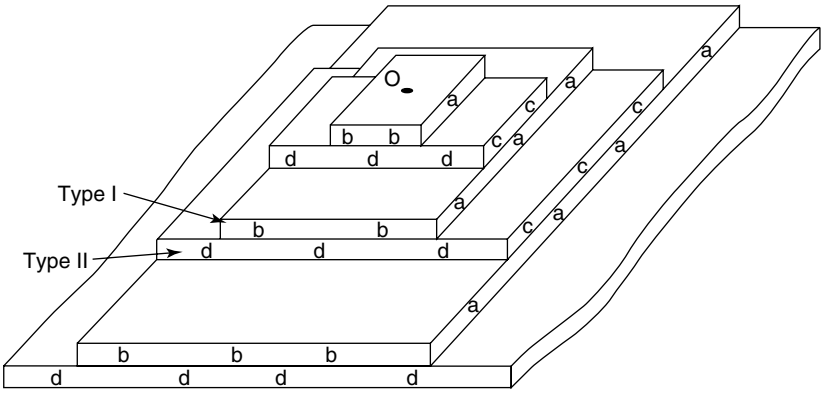

Figure 1.7 Interlaced spiral formation. Figure modified from van Enckevort *et al*. [14].

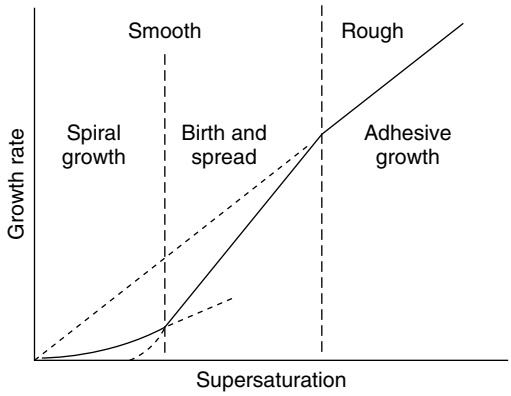

Figure 1.8 Mechanisms of growth as a function of supersaturation.

birth and spread, or spiral growth. A surface will transform from smooth to rough at high driving force conditions (high supersaturation). Figure 1.8 shows the different growth mechanisms as a function of supersaturation. At a low supersaturation, the interface is smooth and spiral growth is the mechanism of growth. After reaching a critical supersaturation for 2D nucleation, birth and spread dominates the growth. In these two domains crystals are bound by crystallographically flat faces with polyhedral morphologies. At high supersaturation the surface transforms to a rough interface, and adhesive-type growth dominates. In the adhesive-type regime the energetics of growth unit attachment are the same regardless of the crystallographic direction, giving rise to crystals bounded by rounded noncrystallographic surfaces, producing spherulitic, fractal, and dendritic patterns.

1.3
Nucleation and Growth in Zeolites

1.3.1
Overview

Zeolite and zeotype synthesis is well known to be a complex process. The rate of crystallization, types of products formed, and their particulate properties (habit, morphology, and crystal size distribution) depend on a large number of parameters [21]. These parameters encompass the crystallization conditions (temperature, stirring, seeding, and gel aging) as well as composition-dependent parameters (pH, water content, and the ratio between framework-forming elements, template concentration, and ionic strength). Nevertheless, a typical zeolite/zeotype synthesis will involve the following steps [22]:

1) A mixture of amorphous reactants which contains the structure-forming ions (such as Si, Al, P, Ga, Zn, etc.) in a basic medium (although a few zeolite synthesis can also take place in acidic medium [23]). This leads to the formation

of a heterogeneous, partly reacted phase, which has been referred to as the *primary amorphous phase* [22, 24]. The nature of this amorphous phase ranges from gel-like to colloidal in the so-called clear solution synthesis [25, 26].

2) Heating of the reaction mixture (above 100 °C) at autogenic pressures in metal autoclaves. Prior to this the reaction mixture may be left for aging for a period of time (hours to a few days).
3) Formation of a ''secondary amorphous phase'' at pseudo-equilibrium with a solution phase [22]. Evidence exists that this phase possesses some short range order due to the structuring effect of cations in the solution [24, 27–30].
4) After an induction period the formation of nuclei takes place. This induction time can be related to the definition for simple systems given in Eq. (1.8) [31]. The relaxation time (t_r) would be the time required for steps 1–3 to take place, that is, for the formation of the quasi-steady state amorphous solid, whereas t_n and t_g have the same meaning.
5) Growth of the zeolite material at the expense of the amorphous solid.

These steps are well defined for a multitude of zeolite and zeotype syntheses, but in many cases it may be difficult to differentiate them. This could be because some of the steps overlap or because the experimental difficulties in studying the synthesis are excessive [22]. Steps 1–3 have been studied in the last several years by many authors. It is not the purpose of this chapter to deal in detail on this subject but the reader is directed to the review by Cundy and Cox [22] for additional information and references.

Figure 1.9 shows the typical shape of a crystallization curve for a zeolite synthesis where both the nucleation rate and the evolution of the crystal-length or crystallinity in the system are plotted as a function of the synthesis time. It can be seen that nucleation only takes place after an induction time, that is, after steps 1–3 have taken place. The rate of nucleation increases rapidly but then decreases to zero. After a certain number of nuclei have formed crystal growth takes place. Initially the

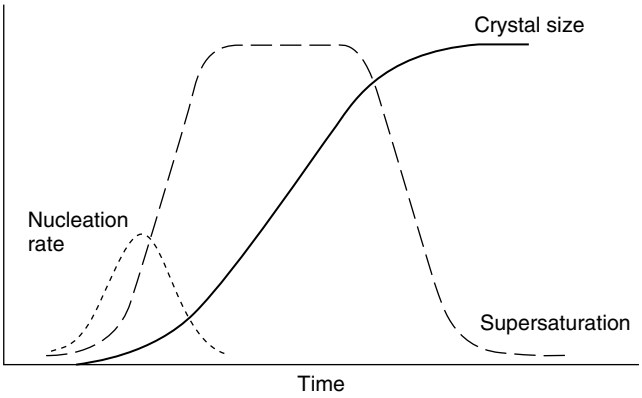

Figure 1.9 Schematic representation of the zeolite synthesis process showing the evolution of nucleation and growth rates, as well as supersaturation, as a function of time.

growth rate increases exponentially but rapidly achieves a steady state before finally decreasing to zero when the nutrients are exhausted. The synthesis process can also be followed according to the theoretical supersaturation curve (superimposed in Figure 1.9). The supersaturation increases initially giving rise to the nucleation and growth phase, then it levels off, as the growth rate achieves a steady state, and finally decreases to zero as all the nutrients in the solution are incorporated into the growing phase.

1.3.2 Zeolite Nucleation

Zeolite nucleation is a complex problem, since it implies the transformation of an initially amorphous or random structure into a crystalline framework. As observed before, during the formation of the secondary amorphous phase there is an increase in the structural order although of very short range. From this step a random number of structured areas may achieve the size of a nucleus and start to grow into a macroscopic crystal.

The use of traditional nucleation theory for studying zeolite nucleation has been employed in the past, for example, in calculating the nucleation rate as the inverse of the induction time [32]. Nevertheless it has been observed that there may be important differences between zeolite crystallization and that of more condensed phases. One of these differences may stem from the high internal surface area of zeolites [33].

The process of zeolite nucleation has proved to be difficult to study and analyze owing to the experimental difficulties in making *in situ* measurements. Various authors have obtained information by using the size distribution and using mathematical models [34] to infer the growth and nucleation rate [21, 35, 36]. Other studies have looked at the effect of aging and seeding on zeolite nucleation. Aging of the initial solution has proved to have influence on the final crystal distribution [22], and hence it can provide valuable information on the nucleation mechanism as has been demonstrated for zeolite A [37] and silicalite [38]. The use of seeds can be the factor used to differentiate between primary and secondary nucleation [22].

Some of the most heated debate on the study of nucleation on zeolite and zeotype synthesis has been centered on the nucleation mechanism, whether this is homogeneous [36, 39] or heterogeneous [40] (primary nucleation) or even secondary [41] (crystal induced). Difficulties in discerning one mode or other stem in part due to the very nature of the gel phase, especially in the so-called clear solution system where it is physically difficult to separate colloid-sized gel particles from the aqueous phase [22]. Nevertheless, there appears to be a growing body of studies supporting the idea that nucleation occurs mainly in a gel phase, specifically at the solution–gel interface [29, 42] where the nutrient concentration gradients are probably the highest. Recent studies on clear solution synthesis have also demonstrated that nucleation actually takes place inside the colloid-sized gel particles [26, 43–45].

The mechanistic aspects of the nucleation process have also been extensively discussed and it is accepted that the process of progressive ordering inside the gel is conducted through a reversible mechanism of breaking and remaking the chemical bonds in the framework catalyzed by hydroxyl ions [46, 47]. Cations and organic-structure-directing agents also have a crucial role in the nucleation process by surrounding themselves with metal-oxide species in preferred geometries owing to electrostatic and van der Waals interactions [48, 49].

1.3.3 Crystal Growth on Zeolites and Zeotypes

A multitude of studies have been carried out to study how zeolite and zeotype crystals grow. Surprisingly, in spite of the vast number of structure types, framework composition, and synthesis procedures, it has been generally found that zeolite growth increases linearly during most of the crystallization process. This is true for both gel synthesis [1, 50–55] and clear solution synthesis [56–59], although studies on the latter system have shown a dependence of the growth rate on the crystal size for values below 15–20 nm [60]. Zeolite growth has been found to be affected by a multitude of parameters such as temperature, gel composition, agitation, and aging, and many studies have been devoted to these topics [1, 22]. In general, measured growth rates of zeolites are consistently lower than those of more dense phases (such as ionic crystals), which has been postulated as due to the more complex assembling mechanism of the open-polymeric structure of zeolite and zeotypes [22].

The fact that the growth rate proceeds linearly almost to the end of the synthesis has been used to support the idea of a surface-controlled mechanism [21, 61]. This idea has been supported by the measured values of activation energies for the growth process, which vary between 45 and 90 kJ mol^{-1} [21, 62–64]. These values are much higher than those corresponding to a diffusion-controlled mechanism [21].

The quest for understanding the true growth mechanism and its fundamentals has been recently aided by the development of new high-resolution surface-sensitive techniques such as AFM [65–67], high-resolution scanning electron microscopy (HRSEM), [68], and high-resolution transmission electron microscopy (HRTEM) [69, 70]. Additionally, new developments in liquid- and solid-state NMR as well as mass-spectrometry techniques shed new light on the physical and chemical nature of the growing units [70]. Furthermore, advanced modeling techniques and theoretical studies have been used to further validate the experimental observation and to provide more insight into the molecular aspects of crystal growth [67].

AFM studies on zeotypes and zeolites were initially limited to the study of natural zeolites [71–75]; nevertheless, in the last several years, numerous studies on synthetic materials have been published [65–67, 76–82], including some on zeotypes [83–85]. Most of these studies have been *ex situ* where crystals were removed from the solution used for growth before analysis but a few *in situ* dissolution studies have also been performed [86, 87].

Initial AFM studies were focused on natural zeolites obtaining high-resolution images of the zeolite surface, so its porous structure could be observed at the surface termination [71, 72, 75]. Nevertheless, in 1998, Yamamoto *et al.* [73] published images of natural heulandite crystals that showed the presence of steps suggesting a possible birth-and-spread mechanism. On the synthetic front, Anderson *et al.* [88] published the first AFM study of zeolite Y, which showed also the formation of steps and terraces on the crystal surface. These studies have been followed by others dealing mainly with zeolite A [67, 77, 87, 89], and X/Y [78, 90] and silicalite [81]. From these investigations, detailed information on the surface termination, the mode of growth, dissolution, and the possible identity of the growth units has been inferred. Until recently, most AFM studies have only revealed the presence of steps and terraces, making some authors to conclude that birth and spread may be the preferential mode of growth for these materials [22]. Nevertheless, a recent study on zeolite A [91] and stilbite [74] shows the formation of spirals. Also, results highlighted in this chapter show that spiral growth in zeotype structures may be more prevalent than originally thought.

1.4 Techniques

1.4.1 The Solid Crystal

1.4.1.1 AFM

The AFM is a surface-scanning technique invented by Binning *et al.* [92] in 1986 as a development of the scanning tunneling microscope (STM) [93]. The AFM provides three-dimensional images of surfaces by monitoring the force between the sample and a very sharp tip (a few nanometers wide). This is in contrast to the STM, which relies on the formation of a tunneling current between the tip and the sample. Therefore, the AFM can be used to scan the surface of virtually any kind of material. Typically, the sample is mounted on a piezoelectric scanner, which moves the sample in x–y and z. The lateral resolution is limited by the tip radius, which normally varies between 10 and 30 nm (although it may be as low as 3 nm), whereas the vertical resolution is around 1 Å, making it ideal to observe small surface details such as steps or 2D nuclei. The end of the tip is attached to a cantilever, which bends when the force between the sample and the tip changes. The deflection of the cantilever is monitored by shining a laser on its top surface, which is reflected back to a photodiode detector. The output signal of the photodiode is then transmitted to a computer. A feedback control system informs the piezoelectric scanner of any changes in force between the tip and the sample, allowing it to alter the tip–sample separation to maintain the force at a constant value.

There are different imaging modes available when using AFM depending on the motion of the tip over the sample. In contact mode, the tip is raster scanned

over the sample while the cantilever deflection is kept constant using feedback control. Intermittent contact mode utilizes an oscillating tip and monitors the phase and amplitude of the cantilever [94]. In this mode the contact between the tip and sample is minimized, and hence may be advantageous for softer samples (e.g., biological samples). Some AFMs can monitor both the vertical and lateral forces (and friction) [95], known as *friction force microscopy* (FFM). In this case, information on the adhesion, friction, or other mechanical properties of the sample can be obtained [96].

The use of AFM has revolutionized the study of crystal growth in the last several years, not only due to its high vertical resolution, but because of its ability to scan in fluids, thus making it possible to monitor *in situ* dissolution and growth processes. AFM has been extensively used in crystal growth studies of macromolecular crystals [97], minerals [98–100], ionic crystals [101, 102], organic semiconductors [103], thin films [104], hierarchical porous materials [105], and many other crystal systems. The use of AFM in studying synthetic zeolites and zeotypes has been slow to come, mainly due to two reasons: (i) the limitations of studying micrometer-sized crystals using a conventional top-head low magnification ($< 20\times$) optics makes locating good crystals very time consuming; (ii) the fact that most zeolites crystallize at temperatures above 100 °C. Nevertheless, the development of tip-scanning AFMs coupled with high-magnification (up to $100\times$) inverted optical microscopes plus new developments in temperature-controlled fluid cells have immensely increased the range of observations that can be made using these systems. This is further illustrated in the six case studies presented in this chapter.

1.4.1.2 HRSEM

Scanning electron microscopy is a well known and used technique for the characterization of microporous materials. It has long been used in conjunction with X-ray diffraction (XRD) as one of the main tools in the studies of crystal growth in zeolites [1, 22]. Its use though has been limited to study the habit, morphology, and size of the synthesized materials but not to characterize the surface detail. This is due to resolution limitations owing to excessive charging on steps at the crystal surface. In recent years, the development of low voltage field emission electron sources for SEMs (FE-SEM) has significantly reduced this issue. For example, in 2005 Wakihara *et al.* [89] reported SEM images of zeolite A where steps could be observed. This new kind of SEM has been dubbed HRSEM and has been shown to be able to observe steps as small as 1.2 nm with ease [68]. The use of this technique promises to open a new chapter in the study of crystal growth of nanoporous materials, complementing the AFM and offering nanometer-scale resolution in areas where an AFM tip cannot have easy access (such as twins, intergrowths, and rough surfaces). Some examples of the full potential of this technique are highlighted in some of the following case studies.

1.4.1.3 Confocal Microscopy

During crystal growth macroscopic defect structures often form, leading to intergrowths, twins, and other more exotic extended structures. Knowledge of these

internal structures of the crystals gives a lot of information about the growth mechanism. Very often these macroscopic growth features can be observed with the resolution of an optical microscope. By operating with confocal optics, often with additional fluorescence from probe molecules selectively adsorbed within the nanoporous crystal, these macroscopic features can be illuminated [106, 107].

1.4.2 Solution Chemistry – Oligomers and Nanoparticles

1.4.2.1 Nuclear Magnetic Resonance

In order to understand how crystals grow, it is necessary not only to understand how the solid phase grows but also to understand the chemistry occurring in the solution phase. Unlike molecular crystals, such as those used in the pharmaceutical industry, the building units for nanoporous materials are in constant interchange in solution. The ephemeral nature of the species makes the task of unraveling, not only what is present in solution but also which are the rate-determining steps in the kinetics of this constant interchange, a very daunting task. The most powerful tool for speciation in the solution state is NMR, and this can be used to good effect to monitor ^{29}Si in silicates [108–119], ^{31}P in phosphates, and ^{19}F in fluorides [120]. These are spin one-half nuclei and, as a consequence, tend to yield highly resolved spectra that are amenable to both one- and two-dimensional spectroscopy. By determining connectivities by INADEQUATE and COSY NMR, a large number of species have now been identified (Figure 1.10). The experiment must be carefully set up in order to ensure quantitation [121] and by inserting chemical probes the course of crystallization may be followed by monitoring pH by NMR [122]. ^{29}Si is only about 4% abundant and therefore two-dimensional spectra can take some time to acquire, precluding the ability to follow rapid temporal changes. This problem is further compounded, as spin half nuclei in solution often have long relaxation times that also substantially slow data acquisition. Nonetheless, ^{29}Si spectra of silicate solutions in particular can reveal an enormous amount of information on a plethora of species. Operated in a multinuclear fashion the complete chemistry of a crystallization such as silicoaluminophosphate (SAPO)-34 [123] may be followed. Quadrupolar nuclei, such as ^{27}Al [124] and ^{17}O [125], can also play a role in understanding solution chemistry. The spectra, although often less well resolved in terms of revealing multiple speciation, can be collected very rapidly and therefore dynamic information may be extracted. Care must also be taken regarding the degree of condensation of species, because as soon as nanoparticulates/colloids are formed the restricted motion of species starts preventing spectral averaging, which is vital for high-resolution spectra. Not only does the lack of motion broaden spectra but also a continuum of complex species with slightly different T–O–T angles will result in a continuum of chemical shifts causing a broadening that cannot be removed even by magic-angle spinning. However, this apparent downside of NMR can also be used to good advantage. For spin one-half nuclei such as ^{29}Si the spectral broadening is often not so substantial to render the resonances invisible. It is therefore very

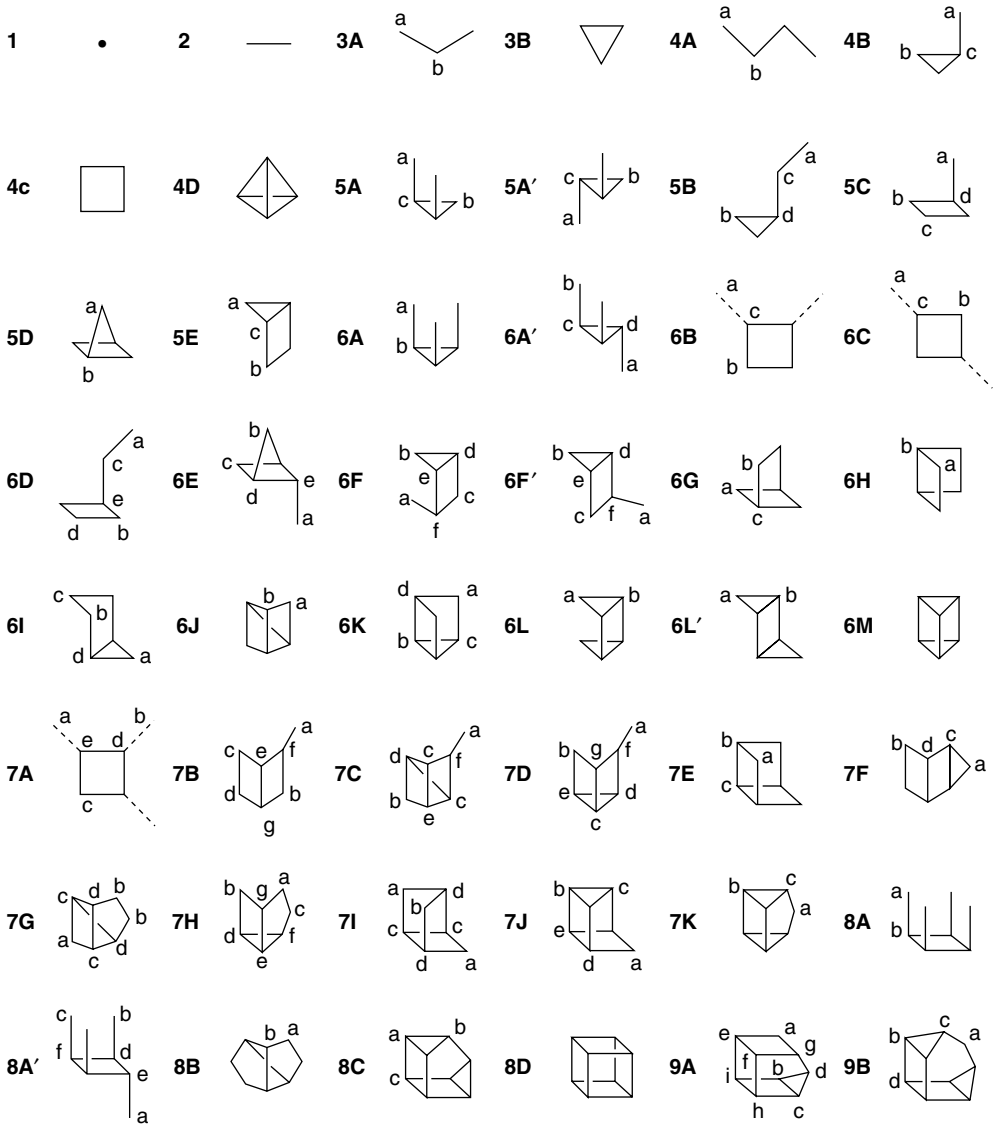

Figure 1.10 Aqueous silicate structures identified in concentrated alkaline solution by $^{29}Si-^{29}Si$ COSY NMR [116].

easy to distinguish between small oligomers, giving rise to sharp resonances, and nanoparticles giving broad resonances. Further, because for spin one-half nuclei quantitation of spectra is straightforward, it is a simple exercise to determine the relative concentration of oligomeric and nanoparticulate species [118, 119] (Figure 1.11).

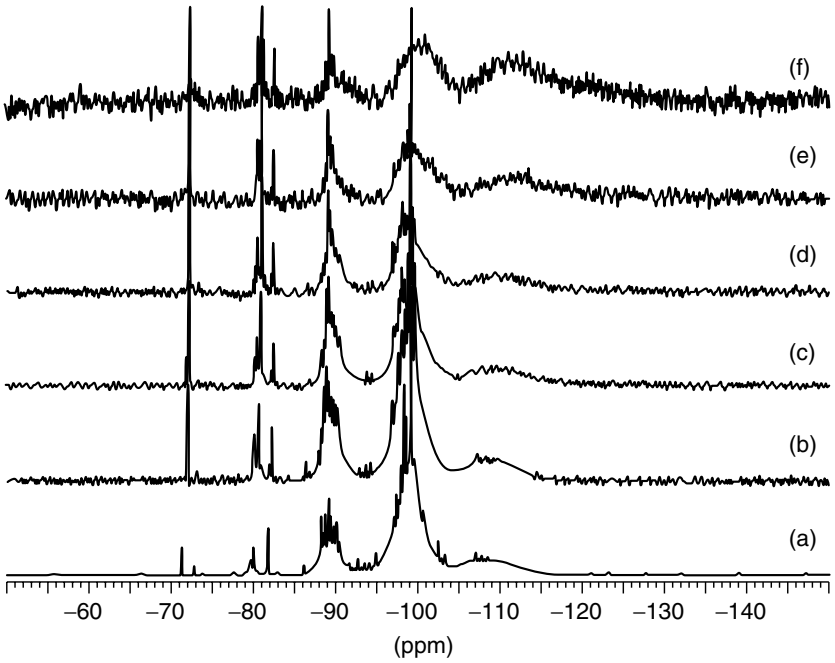

Figure 1.11 Normalized ^{29}Si NMR spectra of clear solutions with TEOS : TPAOH : H_2O molar ratio of 25 : 9 : *x* where (a) *x* 1/4 152; (b) *x* 1/4 400; (c) *x* 1/4 900; (d) *x* 1/4 1900; (e) *x* 1/4 4000; and (f) *x* 1/4 9500 [119].

1.4.2.2 **Mass Spectrometry**

In order to increase sensitivity and temporal resolution, mass spectrometry is becoming increasingly used in the study of solution speciation. Modern mass spectrometers utilizing soft ionization procedures such as electrospray ionization can readily yield parent ions in relatively high mass/charge ratio. Although the speciation is not as unique as that determined by NMR, through isotopic distribution analysis the possibilities may be narrowed considerably. The enormous advantage over NMR is the sensitivity and rapid data collection that permits *in situ* analysis of dynamic events [126–132]. The power of this technique is most aptly demonstrated in a recent work on the interconversion between silicate oligomers [132]. In a clever experiment, a solution enriched with ^{29}Si and a solution of naturally abundant ^{28}Si containing cubic octamers were mixed. The mass spectrometry clearly revealed that the first exchange species contained equal amounts of the two isotopes indicating a concerted exchange mechanism involving four silicon nuclei. A similar experiment with triangular prismatic hexamers showed a concerted exchange of three silicon nuclei (Figure 1.12). Such concerted exchange mechanisms are probably omnipresent in the chemistry of silicates and are likely to play an important role in zeolite crystal nucleation and growth.

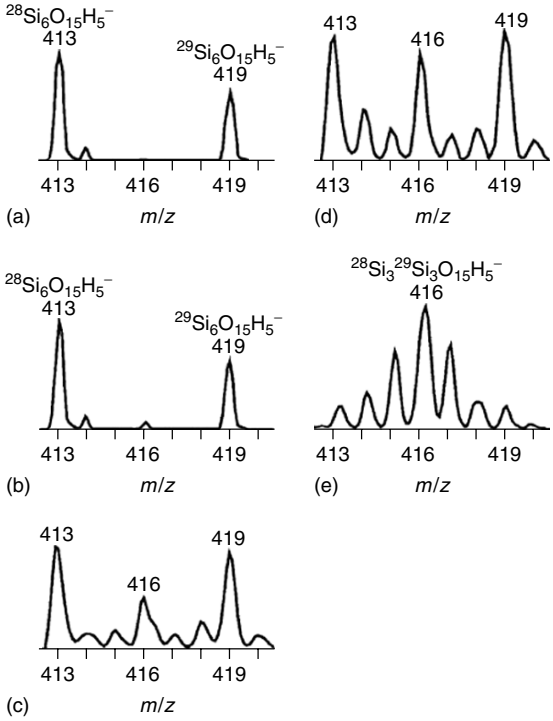

Figure 1.12 Temporal developments of mass spectra after mixing equally concentrated solutions containing the prismatic hexamer with naturally abundant silicon and ^{29}Si-enriched silicon [132].

1.4.2.3 **Cryo-TEM**

The transition from solution to nuclei and finally to crystals is a complicated process to monitor experimentally. Scattering techniques such as dynamic light scattering and X-ray or neutron scattering are able to determine dynamically the presence of important nanoparticulates during these crucial early stages of the birth of crystals. However, recently a new and powerful technique has been added to the arsenal, namely, cryo-TEM. By rapid freezing of the growth medium the nucleation and growth processes may be stopped and the sample transferred, while it remains cold to be analyzed by the electron microscope. This permits high-resolution electron microscopy to be performed on more-or-less unperturbed crystallization media. Recent results on the silicalite system [133] prepared from TEOS and TPA show clearly that the initially formed 5-nm nanoparticulates are amorphous in nature before they agglomerate and crystallize by an intraparticulate re-organization. By performing these experiments in the electron microscope as opposed to utilizing x-ray scattering techniques it is possible to discern the presence or absence of structural order even at these very early stages.

1.4.3 Modeling

1.4.3.1 Monte Carlo Modeling of Crystal Growth

Since the advent of AFM and high-resolution scanning electron microscopy we have a new window to follow the nanoscopic details of crystal growth. In order to interpret these data new tools are required to model not only the crystal morphology but also the details of the surface topology. Monte Carlo techniques provide a possible route to simulation of crystal morphology and topology whereby the structure is developed according to a set of thermodynamic rules. The first problem is to decide which unit to choose as the growth unit. For a molecular crystal the answer is straightforward as the indivisible element in the growth is a single molecule, and Monte Carlo techniques have been successfully used, for instance, for urea [134–136]. For nanoporous materials such as zeolites it is necessary to coarse grain the problem in a way that makes the calculation manageable. This is readily done by realizing that the rate-determining steps in the crystal growth process are related to closed-cage structures capped with Q_3 groups at the surface. Open-cage structures exposing Q_2 and Q_1 groups are highly susceptible to dissolution and as a consequence do not persist at the surface. Having selected the coarse grain as a closed-cage structure, a network of closed cages is constructed and the probabilities for growth and dissolution determined according to the energetics at each site. The methodology chosen is essentially that of Boerrigter *et al.* [137] whereby each site at the surface of a crystal is assigned an energy relative to the bulk phase (see Figure 1.13 for description of energy levels). Growth from solution then occurs through an activated complex, essentially desolvation followed by adsorption, but the energy which defines the relative rate, or probability P, of growth and dissolution, $P_{i2j}^{\text{growth}}/P_{i2j}^{\text{etch}}$, is a combination of the energy of the site (termed *site i2j* in Meekes terminology), relative to the bulk phase, $(\Delta U_{i2j} - \Delta U)$and the supersaturation, $\Delta\mu$ (Eq. (1.11)) [138–140]. The ordering of the energy levels to the first approximation follows the order of the nearest neighbor connectivity, with second-order connectivity resulting in smaller energy differences.

$$\frac{P_{i2j}^{\text{growth}}}{P_{i2j}^{\text{etch}}} = \exp(\beta(\Delta U_{12j} - \Delta U) + \beta\Delta\mu) \tag{1.11}$$

By treating this problem numerically by computer the real meaning of supersaturation and equilibrium becomes immediately apparent. The Monte Carlo treatment is conducted so that growth and dissolution events occur according to Eq. (1.11). The supersaturation may be treated as a constant or variable. By setting up a virtual solution phase which increases in concentration for an etch event and decreases in concentration for a growth event, the supersaturation is allowed to drop freely as the crystal grows. Equilibrium is established when the crystal stops growing and the number of growth and etch events over time are equal. At this point the value of $\Delta\mu$ is determined. Conventionally, $\Delta\mu$ is zero

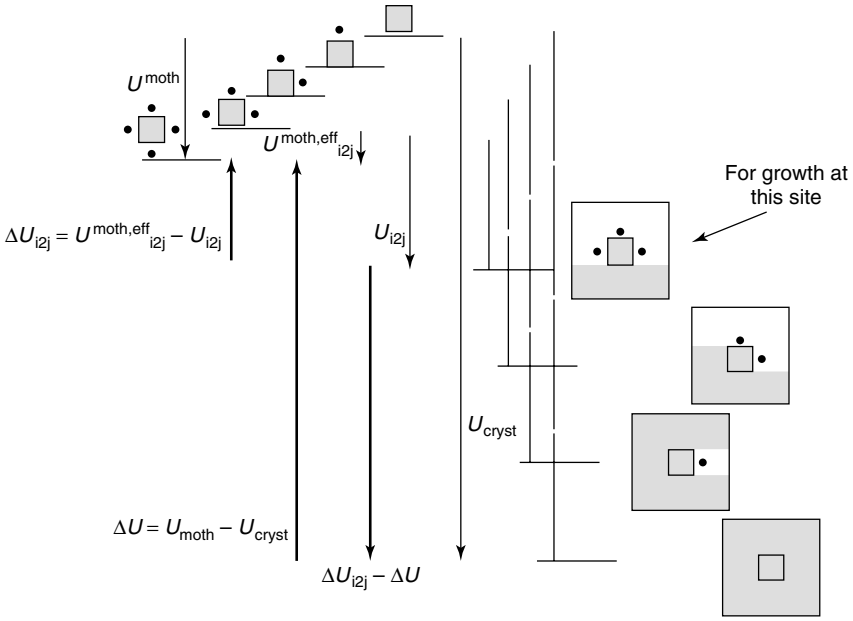

Figure 1.13 Energy level descriptions for growth of crystal from solution. At left is the solvated growth unit in solution. At top is a fully desolvated growth unit in vacuum and at the bottom, the growth unit fully condensed in the bulk crystal. Energy nomenclature corresponding to [137] is given, which relates to the probabilities for growth and dissolution given by Eq. (1.11).

at equilibrium as the conventional definition of supersaturation is the difference between solution concentration and that recorded at equilibrium. However, a much more powerful definition of equilibrium is achieved by considering the value of $\Delta\mu$ relative to the energies of each growth site, ($\Delta U_{i2j} - \Delta U$). At equilibrium some sites will be in undersaturation (the low-coordinate sites) and some sites will be in supersaturation (the high-coordinate sites). Equilibrium is just the balance point, the center of gravity, of energies of all the sites taking into consideration the number of each of those sites. The Monte Carlo approach finds this center of gravity equilibrium state that always lies within the range of the kink sites. It is not a problem that has a ready analytical solution because the number of sites of each type depends upon the specific connectivity of the crystal – in essence it depends on the crystallography of the crystal. For studies of nanoporous materials, this gives a route to study the problem experimentally without worrying about the extremely difficult problem of determining conventional supersaturation of the solution. Crystals may be taken to the equilibrium condition and then compared against the Monte Carlo calculation for the same condition. Figure 1.14 shows examples of crystals simulated under different conditions.

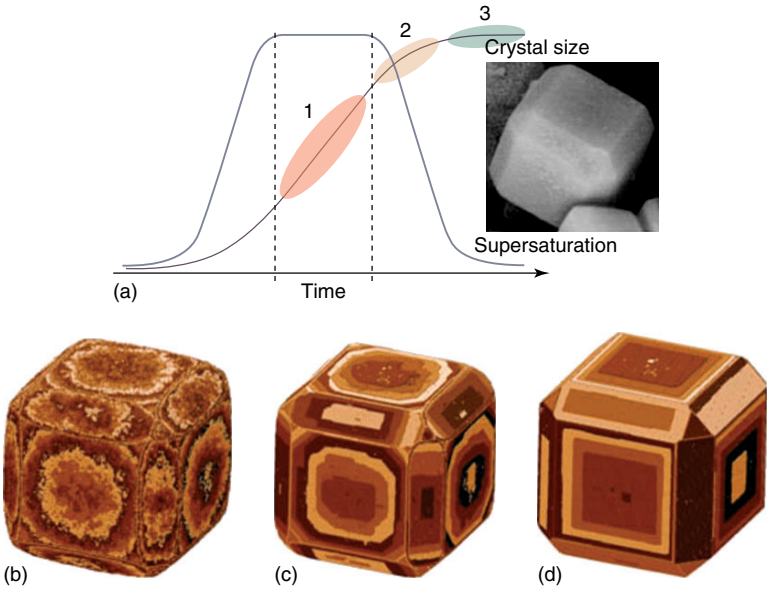

Figure 1.14 Typical crystal size and supersaturation evaluation as a function of time for zeolite A synthesis. Inset SEM picture (image size 2.5 μm) shows typical zeolite A crystal produced in the synthesis. b–d show about $0.3 \times 0.3 \times 0.3\mu m^3$ sized zeolite A crystals simulated at time interval 1, 2, and 3, respectively [138].

1.5 Case Studies

1.5.1 Zeolite A

Zeolite A is one of the most widely used zeolites due to its ion-exchange capabilities [141]. Zeolite A has a framework structure known as *Linde type A* (LTA) [142] consisting of sodalite (SOD) cages linked via four rings, and an Si to Al ratio of 1 : 1. The SOD units join to produce an α-cage with a diameter of 11.4 Å (the large cavity in the center of the structure), and two channel systems which are connected to allow motion of the Na^+ ions and water molecules. Its empirical formula is $Na_{12}[Al_{12}Si_{12}O_{48}]\cdot 216H_2O$. Investigations on zeolite A have been numerous and varied with a multitude of studies focusing on the effect of different parameters in its growth, such as the addition of organic molecules to the synthesis mixture [143, 144], seeding [145], aging [37], and clear solution [25].

Zeolite A has also been the subject of various AFM studies [67, 146, 147], including the first *in situ* dissolution study in a zeolite [87]. These observations were limited to the study of the {100} face in crystals extracted at the end of the synthesis (i.e., a low supersaturation condition), with no information available on

the crystal growth mechanisms under other conditions. A more thorough study has been carried out to study the evolution of the surface features of zeolite A at different synthesis times by means of AFM and HRSEM. Zeolite A crystals were prepared following the preparation of Thompson and Huber [148]. The synthesis was carried out at 60 °C and at the following synthesis times: 2.5, 4, 8, 20, 30, and 50 hours. A second preparation following the method by Petranovskii *et al.* [144] includes the addition of diethanolamine (DEA), an organic molecule whose main effect is to increase the size of the crystals and which also has an effect on the morphology of the crystals. In this experiment, the reaction was carried out at 90 °C and the synthesis times were 12, 16, 20, 24, 28, 32, 36, 40, 44, 48, 72, 96, 120, 168, 336, and 504 hours. The reason behind the much longer experimental times was to observe any possible change in surface topography at long ''equilibrium times'' in order to allow for surface and habit rearrangement.

1.5.1.1 **Thompson Synthesis**

Figure 1.15 shows the evolution of zeolite A synthesized as a function of time. It can be seen that after 8 hours the crystallization is almost complete. At 2.5 and 4 hours the growth rate of the crystals is at its maximum, which also corresponds to the highest supersaturation achieved in the system (Figure 1.9). At 8 hours, however, the growth rate has probably started to decrease, reaching almost zero at 20 hours.

Figure 1.16 shows the corresponding HRSEM of crystals extracted after 2.5, 4, 8, and 20 hours, whereas Figure 1.17 shows the AFM images after 4, 8, and 20 hours. When comparing both images a more detailed picture of the crystallization process emerges. At 2.5 hours (Figure 1.16a) it can be seen that crystals are small (a few nanometers to 400 nm) and rounded, and there is also strong evidence of intergrowth formation and aggregation of crystals. Although no AFM images could be obtained on these round crystals, the HRSEM resolution allows us to see that the crystal surfaces are very rough. All these features are evidence of an adhesive mechanism of growth typical of high supersaturation conditions. At 4

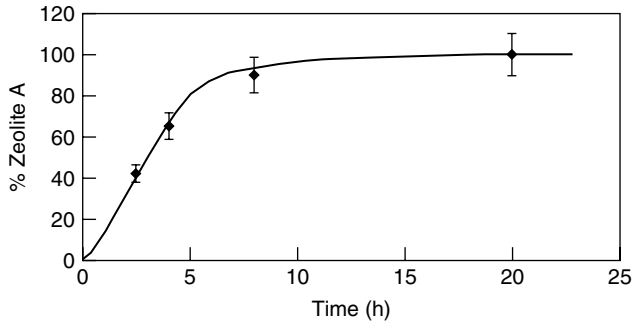

Figure 1.15 Percentage of zeolite A crystallized as a function of time. Superimposed is a theoretical growth curve for this kind of system.

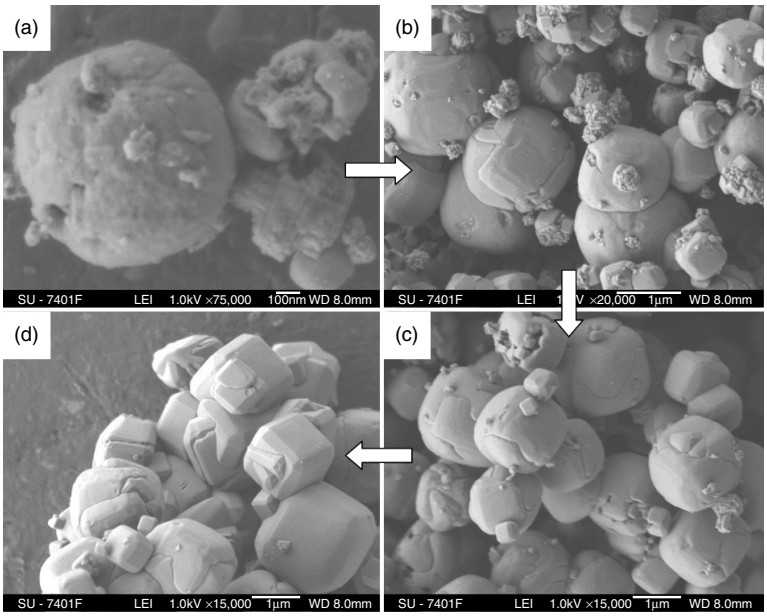

Figure 1.16 HRSEM photomicrographs of zeolite A crystals after (a) 2.5 hours; (b) 4 hours; (c) 8 hours; and (d) 20 hours of synthesis.

hour HRSEM (Figure 1.16b) and AFM (Figure 1.17a) images show a similar picture. At this point of time, crystals are much bigger (up to 1 μm) and still somewhat rounded but they start to show the formation of facets. This can also be seen in the AFM image (Figure 1.17a) where steps start to be visible, although evidence of active 2D nucleation is also present. Eight hours into the synthesis the crystals have grown even more, reaching sizes up to 1.5 μm. HRSEM images (Figure 1.16c) show that the crystals are more faceted than before, although still with rounded edges. The corresponding AFM image (Figure 1.17b) shows well-defined steps and terraces with nucleation limited to the central terrace. This indicates that supersaturation has now dropped and growth takes place by a layer growth or single nucleation mechanism (Section 1.2.12). At 20 hours the crystals are fully developed (Figure 1.16d) and show the typical faceted morphology for this synthesis [149] bounded by {100} and {110} and {111} faces. AFM taken on these samples on the {100} face (Figure 1.16d) agrees very well with what has been published before [67, 89] and displays single square terraces at the center of the face that grow by step advancement toward the edge of the crystal. The steps are almost perfectly rectilinear as well. Figure 1.16c shows the AFM image of a {110} face; it can be seen that in this face the shape of the terrace is rectangular, displaying a faster growth along the <100> direction and slower on the <110>. This situation is indicative of a very low supersaturation and has been successfully replicated in Monte Carlo simulations.

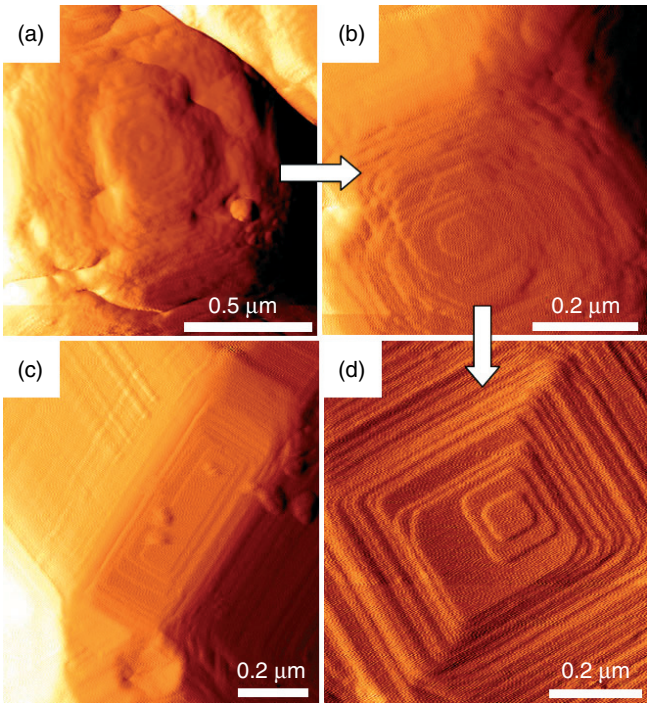

Figure 1.17 AFM deflection images of zeolite A crystals after (a) 4 hours; (b) 8 hours; and (c and d) 20 hours of synthesis. a, b, and d show {100} faces, whereas (c) shows the {110} face.

1.5.1.2 **Petranovskii Synthesis**

Figure 1.18 shows two SEM micrographs of the end product of the synthesis of zeolite A in the presence of DEA at 90 °C. The end product in this case displays a much larger size (up to 15 µm) and the crystals are bound only by the {100} and {110} faces. Also the relative size of the {110} face in comparison to the {100} face is higher for this synthesis.

A detailed AFM study was undertaken to analyze the surface topography of all the samples synthesized. Figure 1.19 shows eight AFM images taken on crystals extracted at 44, 48, 72, 96, 120, 168, 336, and 504 hours after the start of the synthesis. At 44 hours (Figure 1.19a), it can be seen that the crystal surface is still quite rough, indicating that 2D nucleation is still happening at a faster rate. Still SEM analysis on the evolution of the length of the crystals with synthesis time shows that at this time the reaction is almost complete, so supersaturation has already started to decrease. This is reinforced by the fact that at 48 hours, 2D nucleation rate has decreased to the point that the steps and growing nuclei can easily be resolved with the AFM (Figure 1.19b), although nucleation still occurs on narrow terraces. At 72 hours, AFM analysis (Figure 1.19c) shows fewer nuclei at

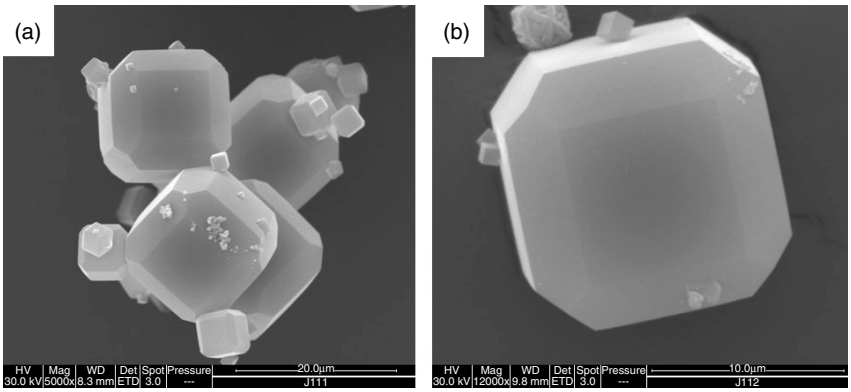

Figure 1.18 SEM photomicrographs of zeolite A crystals extracted after 120 hours of synthesis.

the surface in accordance with the gradual decrease in supersaturation expected at this point of the synthesis. Note that all the terraces are bounded by straight steps with sharp corners. Figure 1.19d–f show the central area of different {100} faces. In the three images a similar situation is observed, where nucleation has almost stopped but the terraces still possess sharp corners. Further into the synthesis, at 336 hours, there is a change in the shape of the terraces, as can be seen in Figure 1.19g. Now the corners of the square terraces are not sharp but curved. At 504 hours, terraces were found to be also curved at the corners (Figure 1.19h). This effect can be explained by means of the Monte Carlo simulation and corresponds to the equilibrium situation explained in Section 1.4.3.1. Since the ''center of gravity'' equilibrium state is located around energies of the kink sites, steps would ''evolve'' toward a shape composed mainly of these sites, resulting in some dissolution and rounding of the terrace corners.

Zeolite A has been dissolved *in situ* using a mild sodium hydroxide solution [87, 150]. Under *in situ* conditions, it is often possible to capture the less-stable surfaces, which tend to be absent if the crystal is removed from the mother-liquor. All *ex situ* measurements on zeolite A have revealed a terrace height of 1.2 nm. However, these terraces dissolve in two steps according to different mechanisms and on different timescales. Figure 1.20 shows an AFM image selected from an *in situ* series which captures both structures. A 0.9-nm terrace is observed dissolving by terrace retreat and a 0.3-nm terrace remains undissolved on the same timescale. The explanation of these results is that SOD cages, 0.9-nm high, which are interconnected, dissolve in a correlated fashion by terrace retreat. One cage must dissolve before the next one can. Single four rings, 0.3 nm, dissolve on a different timescale in an uncorrelated fashion as they are not connected to each other. These results further reveal the importance of closed-cage structures, two of which are seen in this experiment, the SOD cage, and the double four ring.

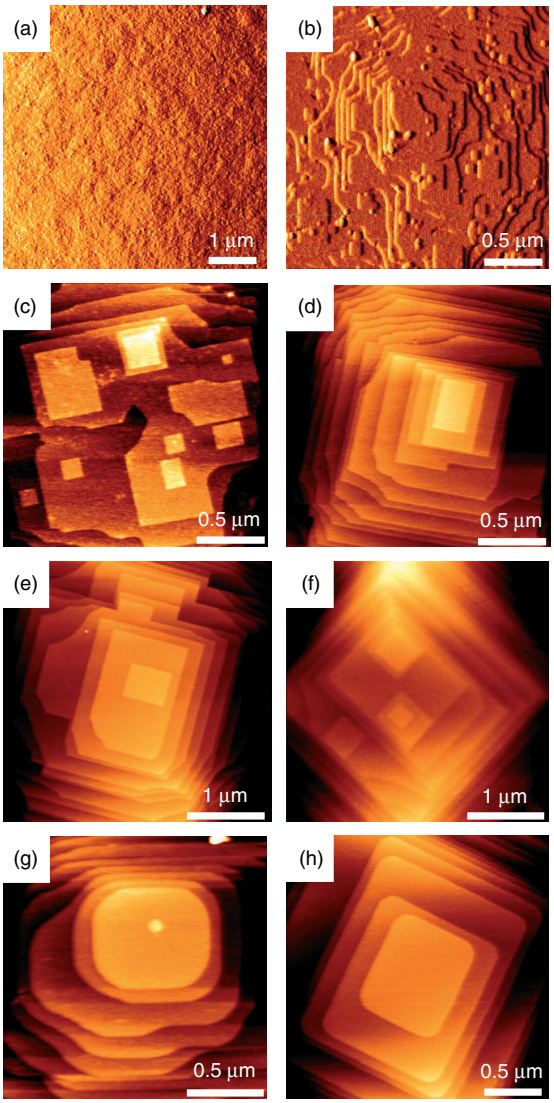

Figure 1.19 AFM deflection (a, b) and height images (c–h) of zeolite A crystals after (a) 44 hours, (b) 48 hours, (c) 72 hours, (d) 96 hours, (e) 120 hours, (f) 168 hours, (g) 336 hours, and (h) 504 hours.

1.5.2 Silicalite

Silicalite is often used in fundamental studies of zeolites owing both to the importance of the MFI structure for catalysis through ZSM-5 and also because of the simplification afforded by having a pure silica framework with no charge-compensating

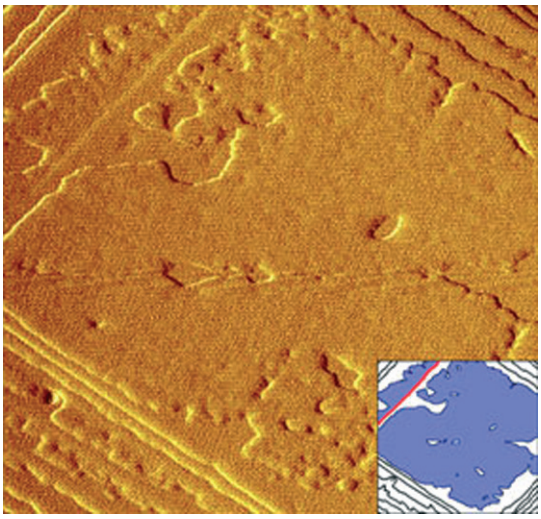

Figure 1.20 4.3 × 4.3 mm^2 deflection AFM micrograph of a zeolite A crystal under static solution of 0.5 M NaOH from *in situ* measurement after 33 minutes. Inset blue area shows 0.9 nm terrace and white area 0.3 nm terrace.

cations. From a crystal growth point of view it also presents an opportunity to investigate (i) the role of templates as the tetrapropyl ammonium cation is such a strong structure director and (ii) the role of intergrowth formation to the MEL, silicalite-2, structure.

Both MFI and MEL structures are composed of connected pentasil chains that can be connected either via a mirror plane or an inversion center. Different choices result in the two structures and this is most readily controlled via structure directing agents that register with the resulting channel system. All AFM measurements to date, on either system, show that the fundamental growth step height is 1 nm, consistent with the pentasil chain unit, thereby conferring an important status upon this closed structure on the growth mechanism.

In a study on the effect of supersaturation, a series of silicalite samples were prepared in a semicontinuous synthesis [151]. Untwinned seed crystals in their spent mother-liquor were placed in a continuous feed reactor. After the slurry reached equilibrium, the nutrient feed was switched on and varied to maintain a constant crystal growth of 0.4 $\mu m\ h^{-1}$. The reaction was continued for a total of 64 hours. During the reaction time, the nutrient feed was stopped for periods of about 16 hours each at 4.3, 9.6, and 16.4 hours, and the supersaturation allowed to drop such that the growth of the crystal more-or-less ceased. The AFM was recorded on each of these crystals, and this is shown in Figure 1.21. During the periods of constant growth the supersaturation level is relatively high and the surface of the crystal is characterized by having a high density of growth nuclei. The crystal grows exclusively via a birth-and-spread mechanism. As the supersaturation drops, when the nutrient feed is turned off the terraces continue to spread but surface

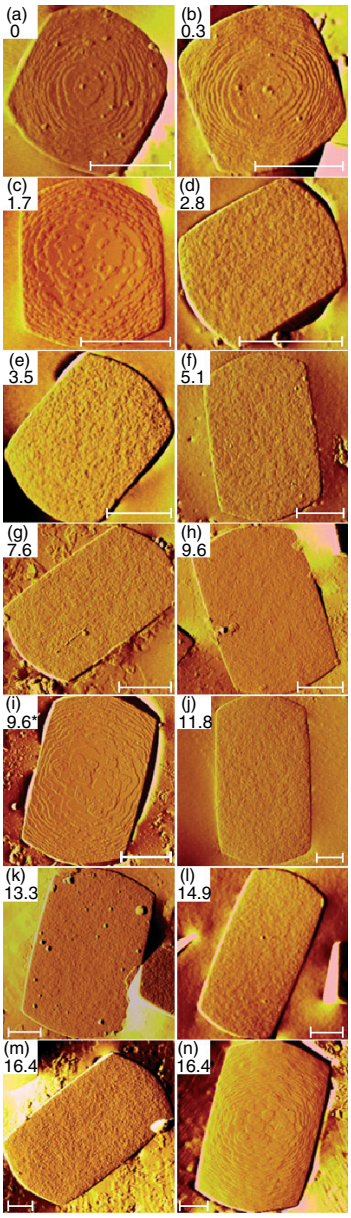

Figure 1.21 AFM deflection images of {010} faces of the silicalite samples. Crystal shown in (a) corresponds to the seed crystal; (b–h) and (j–m) are crystals that were recovered from the reactor under continuous feed. Crystals shown in (i) and (n) were recovered from the reactor after periods of 16 hours when the nutrient feed was switched off and are denoted by 9.6* and 16.4* hours. Time is expressed in hours. The scale bars represent 1 mm [151].

nucleation more-or-less ceases. The reason for this is that surface nucleation requires the highest energy, see Eq. (1.11), or highest value of supersaturation. Near equilibrium the relative rate of growth to dissolution, $P_{i2j}^{\text{growth}}/P_{i2j}^{\text{etch}}$, will be less than unity, and consequently as soon as an entity grows on the surface, it will immediately dissolve back into solution. Conversely, terrace spread is dependent upon lower coordinate, edge and kink sites for which $P_{i2j}^{\text{growth}}/P_{i2j}^{\text{etch}}$ will be closer to or above unity permitting the terraces to continue spreading. The process is reversible as surface nucleation and crystal growth continue when the supersaturation is subsequently raised.

This supersaturation control experiment demonstrates the ability to switch on and off specific crystal growth processes. Such a phenomenon could be used to control defects and intergrowths in zeolites. Zeolite intergrowths in zeolites often result from layer growth, whereby a new layer has more than one choice with similar energy (e.g., an ABA stacking rather than an ABC stacking). If there is a high density of surface nuclei present on any given surface, then there occurs a high probability that some of these are of the slightly less favored stacking sequence. Now, one given layer will have a number of C layers mixed in with the A layers, and as the terraces spread a defect will result when they merge as they will be incompatible. A possible route to overcome such defects would be to lower the rate of nucleation, by lowering the supersaturation such that terrace spreading is still very rapid, but the low nucleation density means that the probability of having nuclei of a different stacking sequence is minimized. Hence, the defect density should decrease. Conversely, by working at very high supersaturation the nucleation density will be high and the probability for stacking sequence incompatibilities will also be high leading to a high defect density. Nanoporous materials such as faujasite (FAU), BEA, and ETS-10 grow according to such rules.

In silicalite, stacking sequence problems arise when pentasil chains attach by an inversion symmetry rather than a mirror symmetry. This will result in a switch from the MFI to the MEL structure when the mistake is on the (100) face, but on the (010) face the pentasil chain cannot connect to the ensuing crystal. This slows crystal growth, and large terrace fronts stack up along the foreign pentasil chain until eventually the defect is overgrown leaving a high density of undercoordinated Q_3 silicons within the structure [81].

Lessons on the role of templates can be learned through competitive templating. TPA is known to be a strong structure director for the MFI structure. By increasing the length of the hydrocarbon chain by one unit tetra butylammonium (TBA) cations will be directed toward the MEL structure. However, the TBA cation is too large to fit at every channel intersection, and consequently there is a topological dilution of the template at the growing crystal surface. The effect of this is immediately apparent in mixed TPA/TBA preparations. Greater than 90% TBA is required in the synthesis before there is a substantial incorporation of TBA over TPA with a corresponding substantial switch from MFI to MEL. Indeed even with 98% TBA and 2% TPA there is still a substantial frustration in the growth of the MEL structure (Figure 1.22). In order to have a smoother transition from MFI to MEL, a smaller template is required and *N*, *N*-diethyl 3,5-dimethyl piperidinium iodide

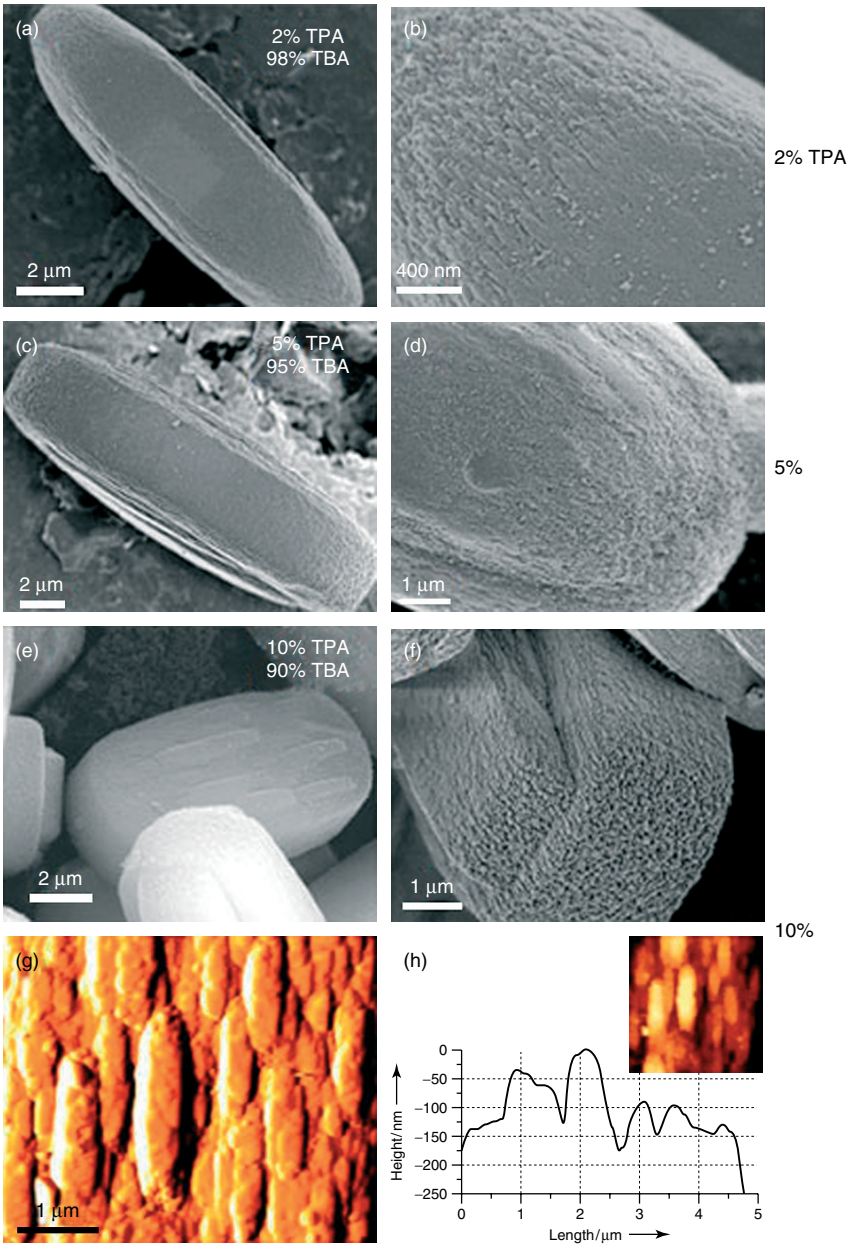

Figure 1.22 HRSEM and AFM images of MFI/MEL intergrowths showing frustration of MEL growth by the incorporation of as little as 2% TPA in the growth swamped with TBA.

(DEDMPI) serves this role. DEDMPI can be accommodated at every intersection and produces MEL crystals that are much less susceptible to stacking sequence problems and the inherent defects.

1.5.3 LTL

Zeolite L has a unidimensional channel structure that typically grows as long hexagonal prismatic crystals with the channels running along the long axis. From a catalytic point of view this is undesirable as the intracrystalline path length for reactants and products is maximized resulting in restricted diffusion. As a consequence, there have been a number of attempts to modify the normal habit to yield tablet-like crystals with a short *c*-dimension. AFM studies of zeolite L [152] reveal the reasons for this crystal habit. Figure 1.23 shows the AFM image recorded on both the hexagonal (001) face and the sidewall (100) face of the crystal. On the top (001) facet the crystal grows via a layer growth, and the smallest height of the terrace is equivalent to the height of one cancrinite cage. The sidewalls show more interesting behavior. Long, thin, straight terraces are observed which are elongated in the *c*-direction of the crystal. Two significantly different heights are measured for these terraces. The narrowest terraces are always 1.2 nm in height

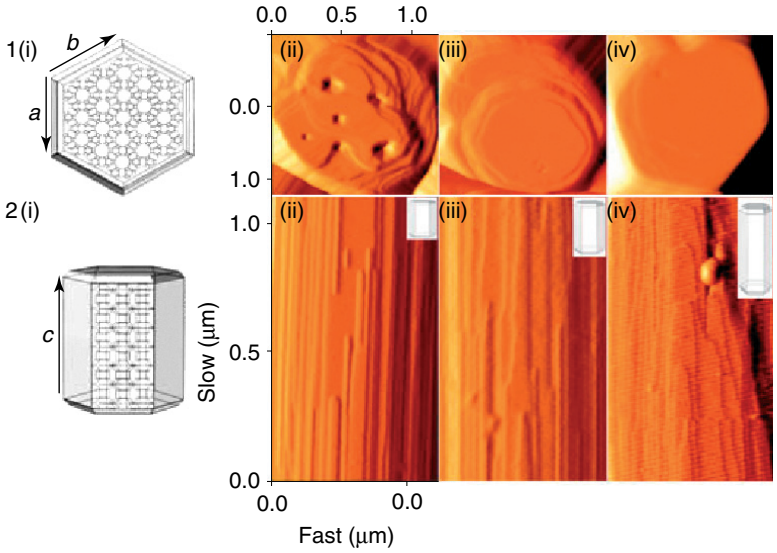

Figure 1.23 Error signal AFM images of zeolite L with different aspect ratios. (1) The hexagonal face down the [001] direction of the crystal and (2) the sidewalls down the [100] direction of the crystal. For each face, (i) shows a schematic framework of the crystal, and (ii), (iii), and (iv) crystals with aspect ratios 1.5, 2.3, and 5.1, respectively.

and the wider terraces are always 1.6 nm in height. The reason for this is that all the narrowest terraces correspond to a single cancrinite column, which grows very rapidly along the *c*-direction of the crystal but is highly frustrated to growth across the side-wall in the *a*- or *b*-direction. Wider terraces are 1.6-nm high because neighboring cancrinite columns are connected by a further cancrinite column that acts as a bridge across the large 12-ring channel. This result illustrates a generic problem to grow crystals with large pores. Circumventing the large pores can result in very unfavorable processes which are more-or-less akin to fresh nucleation. The bridging cancrinite column is more likely to dissolve back into the solution rather than persist until it is secured by the cancrinite column at the other side of the bridge – again according to Eq. (1.11). The problem lies in the fact that two, not one, cage structure is required to circumvent the large 12-ring pore. Growing both cancrinite column structures before one dissolves is an unlikely event, and therefore the kinetics are slow. The traditional way to build nanoporous structures over large void spaces is to add an organic templating agent which facilitates the process; in other words the kinetics for the process are improved. Zeolite L, however, is an example of a wide-pore zeolite that grows readily in the absence of organic-structure-directing agents. Consequently, zeolite L is a good demonstration of how large pore structures can be incorporated into a structure without expensive organic additives, and at the same time this system illustrates where the kinetics are severely frustrated in the process. This frustrated growth also results in the typical long prismatic crystals and the kinetics would need to be adjusted in order to successfully grow low-defect tablet-shaped crystals. Most methods reported to create shorter *c*-dimension zeolite L crystals operate under high supersaturation conditions, where the crystals have a high density of defects and the aspect ratio is only altered as a result of the interrupted growth at macro-defects. Careful adjustment of crystal aspect ratio, while maintaining a low defect density, is yet to be achieved.

Zeolite L is also a very interesting system to investigate, *in situ* by AFM, the mechanism of dissolution. Figure 1.24 shows a series of images recorded as a function of time as the crystal dissolves under mild basic conditions. The micrographs have been recorded in lateral deflection mode, which monitors lateral twist of the cantilever during scanning. This mode is normally used for nanotribology studies as local friction will cause a twist of the cantilever. Three things are immediately apparent from the images. First, the terraces dissolve very rapidly along the *c*-direction of the crystal and very slowly in the lateral direction. Second, the place where the crystal dissolves is bright white, indicating a high degree of lateral twist. In essence, the AFM illuminates where the chemistry on the crystal occurs. This twist is also observed during the growth of nanoporous crystals. Third, it is observed that the bright white region on the dissolving terrace is substantially larger at the top of the terrace when the AFM tip is scanning down the crystal and vice versa. This demonstrates that the tip is aiding the dissolution. The tip in effect warms the crystal. By recording the images at different cantilever loads and temperatures it is possible to make a series of Arrhenius plots, which when extrapolated to zero load (i.e., no effect of the tip) yield the activation energy

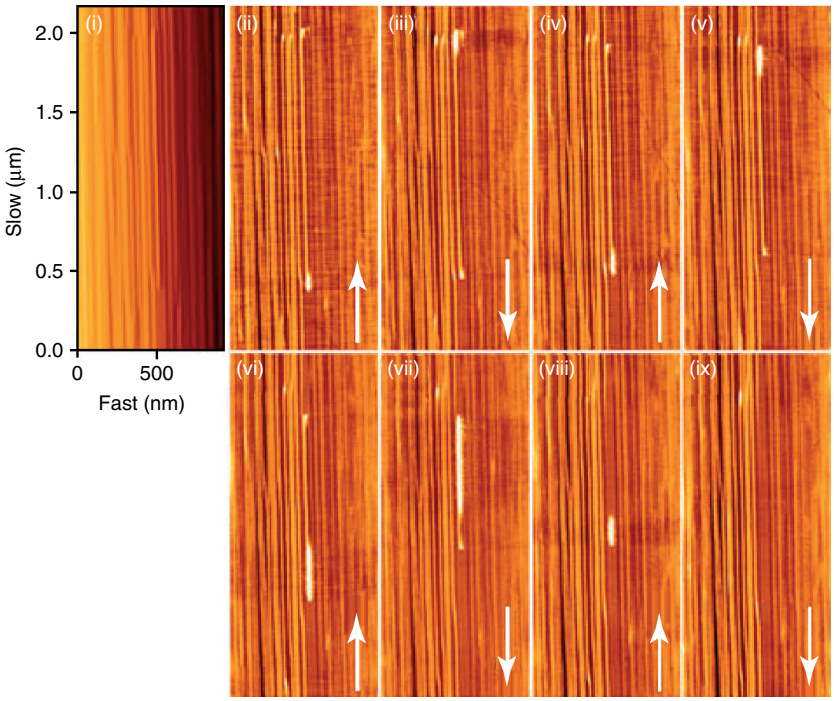

Figure 1.24 Atomic force micrographs of the (100) face of zeolite L during dissolution in 0.2 M NaOH. The image in (i) shows a vertical deflection micrograph at the beginning of the experiment and ii–ix show lateral deflection micrographs on subsequent scans over the crystal surface. The time between each image was approximately 4 minutes. The white "lights" indicate a change in friction experienced by the AFM tip, shown as a high contrast change on the image. The white arrows indicate the direction of scanning.

for this fundamental dissolution process, which is 23 ± 6 kJ mol^{-1}. The cause of the high lateral force is not entirely clear. It could be due to a change in friction when the crystal is undergoing rapid dissolution. However, it also might be due to high local energy being imparted to or from the tip as a result of a large energy change during dissolution. This latter explanation would be consistent with the fact that the phenomenon is observed during both growth and dissolution.

1.5.4 STA-7

STA-7 is a SAPO [153] with the structure type SAV [142]. SAV belongs to a group of four framework structures, composed of double 6-rings (D6Rs), which also includes the frameworks CHA, AEI, and KFI. The only difference between these structures is the arrangement of the D6R along the x, y, and z axes [154]. The SAPO STA-7 structure belongs to the space group $P\,4/n$ and contains two types of cages,

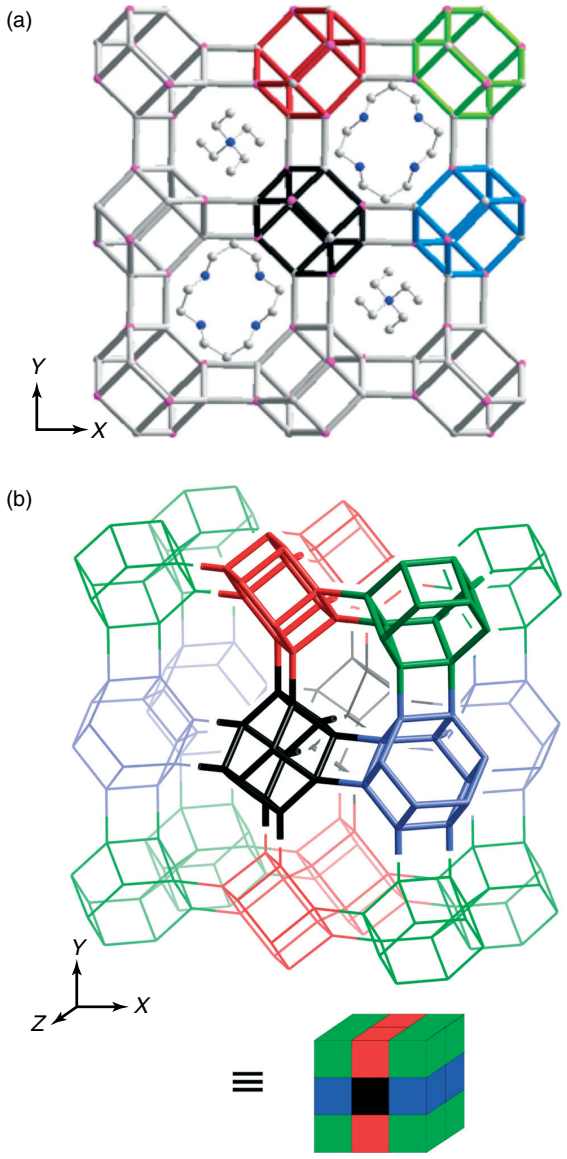

Figure 1.25 (a) STA-7 structure on the {001} face showing the position of the cyclam and TEA molecules inside the two different cages. The four different orientations of the D6R are also highlighted in different colors. (b) 3D view of the STA-7 structure. The four possible orientation of the D6R are highlighted in red, green, black, and blue. The unit cell is highlighted in bold. It can be seen how the units alternate orientation along *x* and *y* directions but not along the *z* direction. A simplified color model of the structure is also shown for comparison.

A and B, connected three dimensionally by eight-ring windows. The larger cage, B, is templated by cyclam and the smaller one, A, by the co-template tetraethylammonium (TEA), as shown in Figure 1.25. In the structure, the D6R units have four different orientations (highlighted in different colors in Figure 1.25) and are related to each other by fourfold symmetry axes and an n-glide plane perpendicular to the <001> direction. Hence, alternating D6R units can be found along the <001> and <010> directions. In contrast, D6Rs form chains along the <001> direction. Consequently, a unit cell consists of two D6Rs along x and y axes, and one along the z axis, as can be seen in Figure 1.25b (highlighted in bold). For simplicity the STA-7 structure can be represented (hereinafter) as a series of cubes of different colors, each one representing a D6R of different orientation (Figure 1.25b).

STA-7 crystals were prepared from SAPO-based gels treated hydrothermally (190 °C for 3 and 10 days). Further details on the characterization can be found in Castro *et al.* [153], but it is important to point out that the formation of STA-7 has proven to be dependent on the presence of the two templates (cyclam and TEA). SEM observations at the end of the synthesis reveal the formation of crystals with a well-defined tetragonal prismatic morphology and with a typical size of 30–35 mm (Figure 1.26a). Therefore, the crystals are bound by two crystallographically distinct

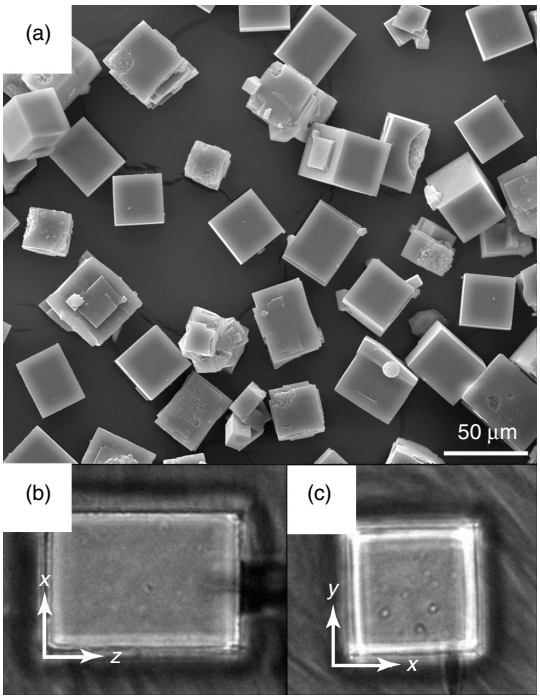

Figure 1.26 (a) Scanning electron micrograph of STA-7 crystals after the end of the synthesis. (b) Optical micrograph of an STA-7 crystal showing the {100} face. (c) Optical micrograph of the {001} face.

faces, {100} and {001} (Figure 1.26b and c, respectively). Both types of faces were characterized by *ex situ* AFM.

1.5.4.1 {**001**} Faces

Figure 1.27a shows a representative AFM image of a {001} face. It can be seen that the surface is covered by multiple nearly isotropic spirals, with all of the scanned surfaces showing a similar dislocation density of approximately 1–2 dislocations per 10 μm^2. No evidence of 2D nucleation was observed, indicating that the system was near to equilibrium when the crystals were extracted. The isotropic morphology of the spirals in this face indicates that there are no preferential growth directions at low supersaturation. Height analysis shows that the step height at the dislocation core (Burgers vector) is always 0.9 ± 0.1 nm (Figures 1.27b,c), which corresponds to the d_{001} spacing, that is, to the height of a D6R along the <001> direction.

Figure 1.8d shows a simplified block diagram of the STA-7 structure, with the different orientations of the D6R highlighted in different colors as described in Figure 1.25b. Rows of similarly oriented D6Rs run parallel to the *z* direction. The original step structure produced by the dislocation is shown by the lightly colored blocks, assuming that the dislocation also runs parallel to the *z* axis with a Burgers vector of 0.9 nm. It can be seen that the sequence of D6Rs on both sides of the dislocation does not change with respect to the normal sequence (green–red–green in the diagram), that is, the bonding through the dislocation between the D6R units is the same as in the undisturbed (nondefective) crystal. Therefore, growth units (assumed to be a D6R) could attach to the step created without modifying the alternation sequence of D6R units along any direction, as represented by the darker colored blocks, perpetuating the STA-7 structure through spiral growth.

1.5.4.2 {**001**} Faces

AFM observations on the {100} faces reveal the formation of two very distinct types of spirals. The first, which is the more numerous one, has an elongated shape, with the long axis, or faster growth direction, parallel to the <001> direction. Height analysis shows that this type of spiral is produced by a dislocation with a Burgers' vector of ≈ 0.9 nm (Figure 1.28a). The second type corresponds to an interlaced spiral (Figure 1.28b,c). The step splitting in this interlaced spiral produces the characteristic ''saw tooth'' pattern (Section 1.2.11) extending from the dislocation, which in this case is parallel to the <100> direction (highlighted by the white box in Figure 1.28c). Height analysis along this pattern reveals that the height of the steps is half a unit cell, that is, 0.9 ± 0.1nm (red line). On the contrary, a cross section from the dislocation center but parallel to the <001> direction (blue line) reveals that the most common step height is one unit cell, that is, 1.8 ± 0.1 nm (i.e., two monolayers). Figure 1.28b shows a higher resolution image of the spiral center, where it can be seen that two single steps (0.9 ± 0.1 nm) emanate from the dislocation, hence the Burgers vector of the dislocation is equal to a unit cell, that is, 1.8 ± 0.1 nm. As explained in Section 1.2.11, an interlaced spiral is produced when each of the different monolayers emanating from the dislocation possesses a different speed anisotropy. In the case of STA-7 this anisotropic growth

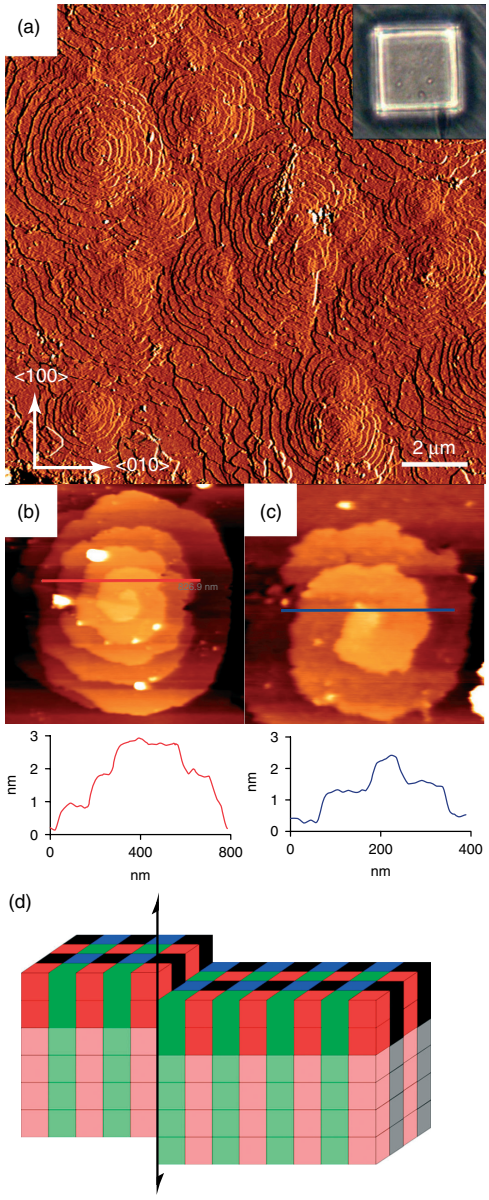

Figure 1.27 (a) AFM amplitude image of a {001} face of an STA-7 crystal. Isotropic spirals in the surface are clearly visible. Inset shows the corresponding optical microscopy image. (b) AFM height image of the lower spiral and cross section. (c) Height image of the upper spiral and cross section. The cross sections were taken along the red and blue lines in the images. (d) Simplified spiral structure after the two new layers have grown. The structure of the newly grown layers matches that of the underlying substrate.

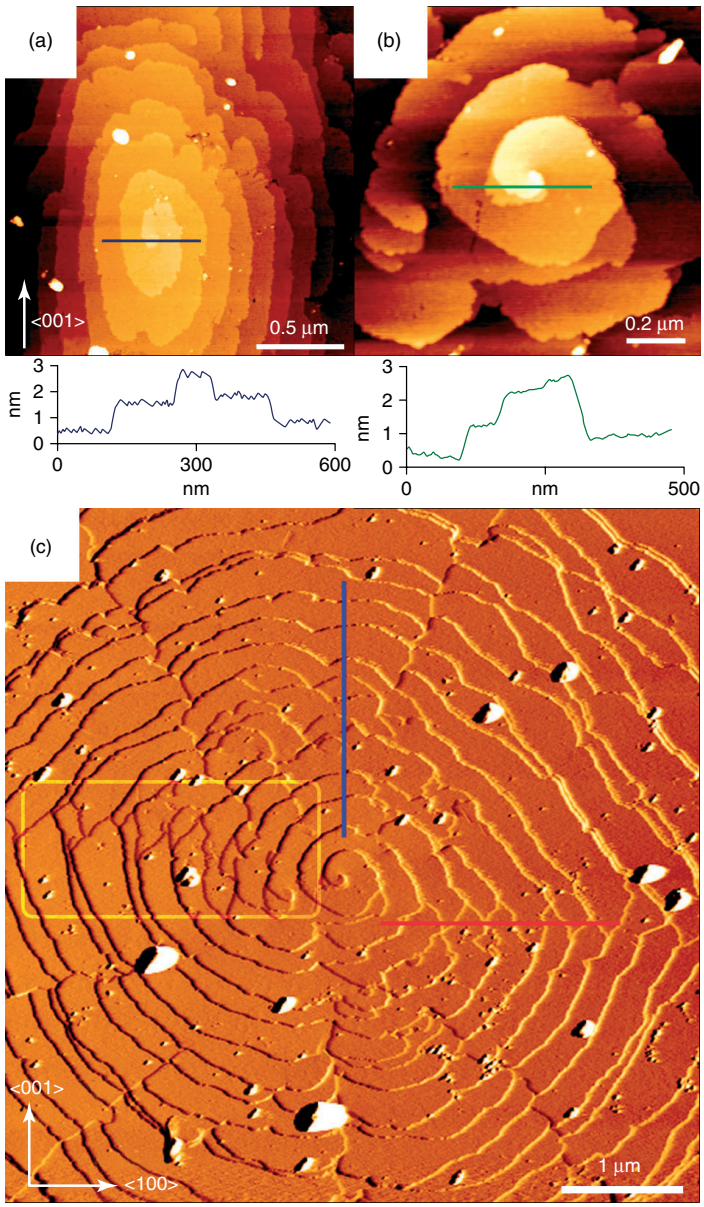

Figure 1.28 (a) AFM height images of an elliptical spiral with cross section. (b) Height image showing details of the central area of the interlaced spiral shown in (c). Two substeps emanating from the dislocation are clearly seen. The cross section confirms the single layer (i.e., 0.9-nm high) nature of these steps. (c) Amplitude image of an interlaced type spiral. Highlighted box contains the characteristic "sawtooth" pattern observed in these types of spirals.

is symmetry-induced due to the presence of an n-glide plane perpendicular to the {100} face. Recently, van Enckevort and Bennema [14] demonstrated that interlacing will be expected when a screw axis and/or a glide plane are perpendicular to the growing surface. The presence of the n-glide plane also determines the shape of the spiral to be symmetrical at both sides of the <100> direction, which marks the intersection of the n-glide plane with the {100} face. Also, the spiral is symmetrical along <001> direction owing to the symmetry axis. By taking into account these symmetry constraints, it is possible to deconstruct the growth anisotropies of the individual substeps. In the case studied, the two substeps show a difference in the growth rates along [001] and [00$\overline{1}$] directions. One substep will grow faster along the [001] direction than along [00$\overline{1}$], whereas the other will be opposite. This situation is summarized in Figure 1.29. Figure 1.29a,b shows a simplified diagram of the two substeps as they would grow if no interference occurred. The anisotropic growth along <001> direction for each substep is clearly evident. In Figure 1.29c, the trajectories of the two spirals are superimposed, demonstrating clearly how they can form the observed interlacing pattern (Figure 1.28c).

The cause of the anisotropic growth can be explained by the tilting of the D6R units with regard to the <001> direction. This tilt can be seen more clearly in Figure 1.30a, which shows a cross section of the STA-7 structure perpendicular to <100> direction. In one layer, D6R units are tilted toward [001] direction, whereas on the following they will all be tilted in the opposite direction, [00$\overline{1}$]. This tilt creates two different step geometries, one acute (red box) and one obtuse (blue box), one of which may favor the attachment/docking of the template preferentially over the

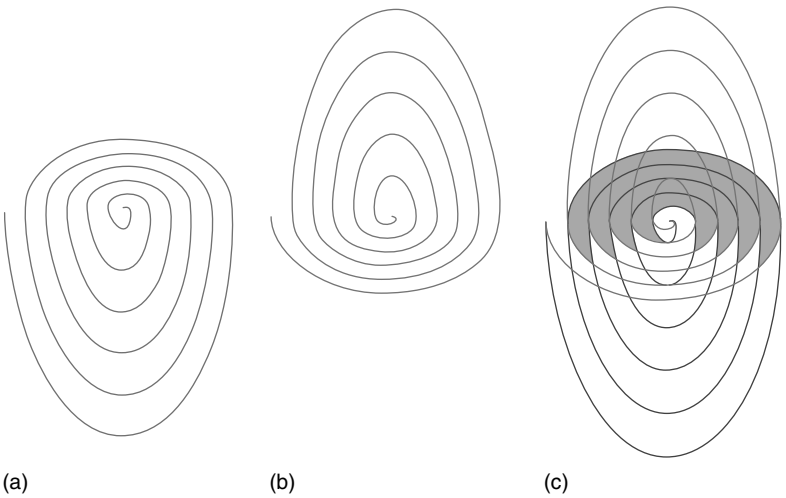

Figure 1.29 Simplified diagrams showing the formation of an interlaced spiral. a and b The assumed shape of each substep if they could grow freely. (c) The overlapping of the two substeps. Here the interlaced pattern is readily observable.

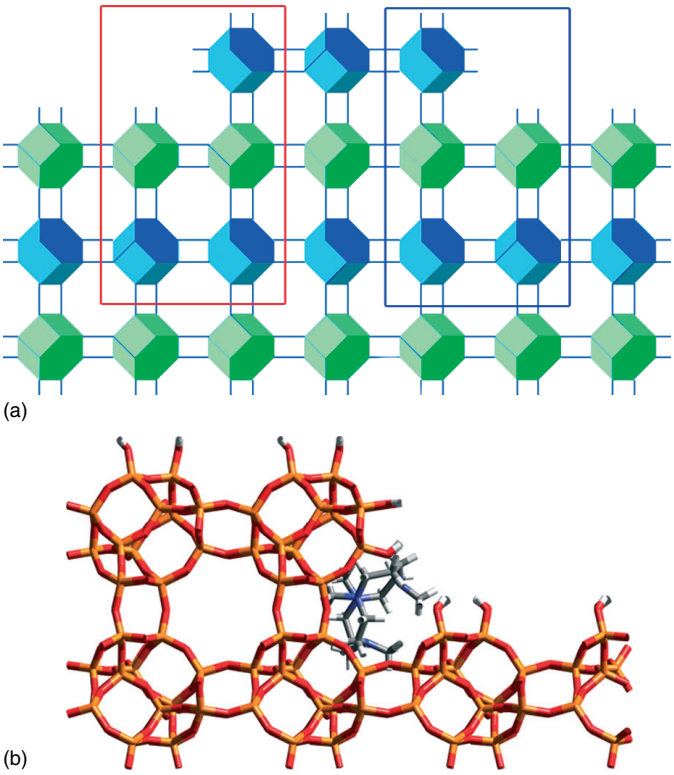

Figure 1.30 (a) Simplified cross section perpendicular to <100> direction, showing the step structure in a {100} face. The two distinct step geometries, acute and obtuse, are highlighted in red and blue. (b) Cross section of the acute step showing the most stable docking configuration for the cyclam molecule after simulation.

other and hence favor the growth along one direction. A similar situation has been observed in calcite crystals where steps are also nonequivalent and ion sorption depends on their geometry [155]. To test this hypothesis, template adsorption at the surface was simulated using an adapted version of the ZEBEDDE program [156] to perform a Monte Carlo simulated annealing (MCSA) [157]. The template adsorption energies (nonbonding) from the simulations suggest that while TEA can adsorb at all adsorption sites with approximately equal energy, the larger cyclam can only adsorb favorably into the large cage site on the "acute" side of the step. Therefore, it is presumed that growth will be favored on the acute step side, where the cyclam accelerates the rate of growth unit attachment relative to the TEA-only mechanism on the obtuse step. As the position of the acute steps alternates between layers as the {100} face grows, the fastest growth direction follows, creating the interlaced pattern. Figure 1.30b shows a detailed cross section of the step structure with the cyclam molecule attached in its more favorable position.

1.5.5 Zincophosphates

Zincophosphate open-framework materials are a class of zeotype materials. In some cases, they show framework types same as those found on zeolites, such as SOD [158] and FAU [159]. However, some possess unique framework types, such as the chiral zincophosphate (CZP) framework, which have no aluminosilicate analog. The zinc phosphates with SOD and FAU structures were first synthesized by Nenoff *et al.* [158] under very mild pH and temperature conditions. However, the synthetic conditions are much milder in the case of the zinc phosphates [160]. These milder conditions are particularly well suited for performing *in situ* experiments on the AFM, as compared to aluminosilicate zeolites. Following results from *in situ* growth experiments on ZnPO-SOD and ZnPO-FAU are discussed.

1.5.5.1 $ZnPO_4$-Sodalite

SOD zinc phosphate, which is synthesized at temperatures ranging from room temperature to 50 °C [158], has a primitive cubic framework, with a unit cell constant $a = 0.882$ nm and belongs to the *P*-43*n* space group. The system contains a 1 : 1 mixture of tetrahedral zinc and phosphorous units that alternates within the framework, giving a stoichiometry of $Na_6(ZnPO_4)_6 \cdot 8H_2O$ [158]. ZnPO-SOD was synthesized following the original room temperature recipe by Nenoff [158]. This produced highly intergrown crystals which were not suitable for AFM experiments. To solve this issue, the synthesis was performed at 6 °C with the goal of decreasing growth and nucleation rates, which may produce better quality single crystals. The synthesis did produce single crystals, as well as intergrowth and the ZnPO-CZP. SOD crystals had dimensions ranging from a few microns up to 15 μm. Crystals were bound by {100}, {110}, and {111} faces. These crystals were attached to a resin and brought in contact with low supersaturated solutions.

In situ experiments performed on the {100} face in contact with low supersaturated solutions revealed the formation of spirals. Figure 1.31a shows one of these spirals. The angles between steps are slightly distorted since the growth rate is too fast for the scan speed to catch up. The overall morphology observed should be a square. Still it can be clearly observed that the spiral formed is of the interlaced type, such as those observed on STA-7, with two monolayers spreading out from the dislocation. In this case, however, the splitting has a fourfold symmetry, which, of course, agrees with that of the ZnPO-SOD crystal studied. Also, it has a polygonal shape, contrary to the rounded contours on the STA-7. Height analysis reveals that each monolayer height is about 0.45 nm, which corresponds to half a unit cell of ZnPO-SOD. Figure 1.31b shows the simplified 3D structure for ZnPO-SOD where a monolayer (highlighted) has started to grow.

The real insight on the crystal growth process that can be achieved by monitoring the process *in situ* is highlighted in Figure 1.32. In this figure, a sequence of lateral force AFM images shows two interlaced spirals growing, and the interlacing-inducing growth anisotropy for each substep can be clearly observed. In Figure 1.32a the two spiral centers are highlighted by white circles. Because of the

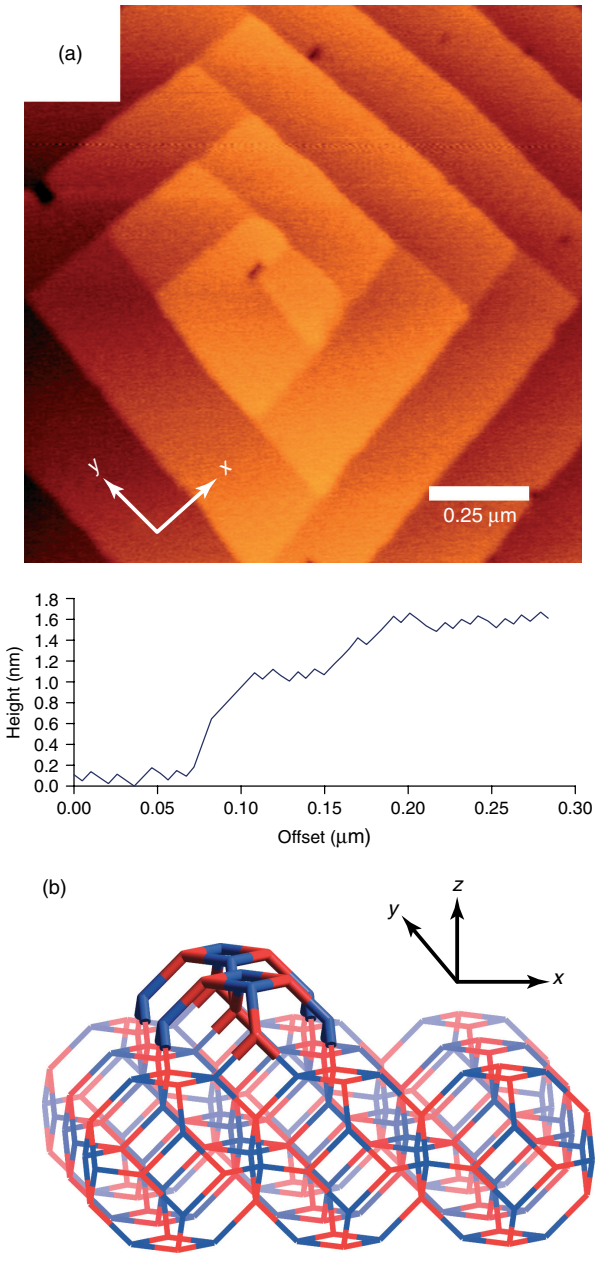

Figure 1.31 (a) AFM deflection image showing interlaced spiral growth on a ZnPO-SOD crystal and associated cross section. (b) Simplified 3D structure of ZnPO-SOD showing the 1/2 unit cell step (highlighted in bold).

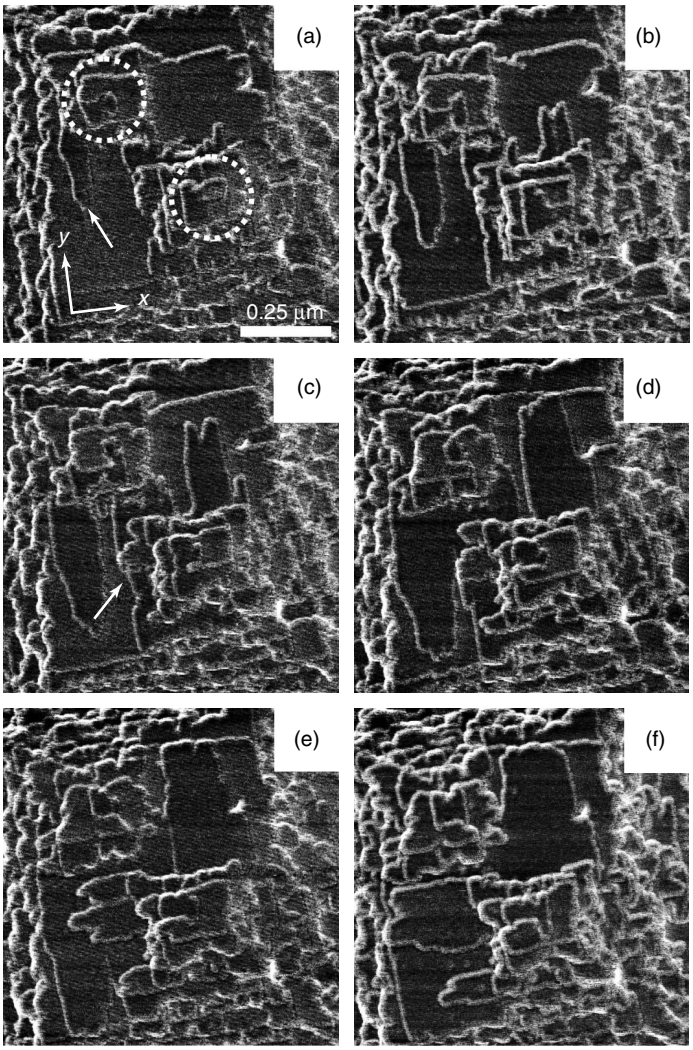

Figure 1.32 Sequence of lateral force AFM images showing the growth of two interlaced spirals.

way in which both spirals interact; two clear square areas are created in between. A white arrow in Figure 1.32a signals the position of a step which can be seen advancing in the following images. The advancing speed of this step is much higher along <010> direction than along <100>. On the contrary, the next step to growth on top (highlighted with white arrow in Figure 1.32c) advances much faster along <100> direction than along <010>, as can be seen on Figure 1.32d–f. Figure 1.33 shows the two interlaced patterns of each step as if they could grow freely (in a similar fashion as in Figure 1.29 for STA-7). It can be seen that the shape of each step would be rectangular because of the anisotropic growth, and how successive

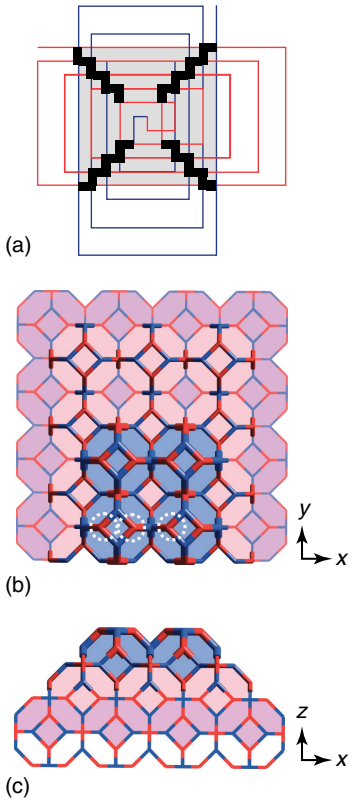

Figure 1.33 (a) Theoretical free development of steps in the absence of interference. (b and c) Simplified structure of ZnPO–SOD showing three different steps (highlighted in different colors) at various stages of growth.

steps will alternate between fast and slow directions. The interference pattern created by two such substeps is the actual pattern observed in the experiments.

The reason behind this anisotropic growth is not fully understood, but it may have to do with the alternation of Zn and P positions in the ZnPO-SOD and the rates of condensation of the two different elements into the structure. Figure 1.33b shows a schematic ZnPO-SOD structure where three monolayers have grown (highlighted in three different colors). The red and blue colors represent Zn and P tetrahedra, respectively. Figure 1.33c shows a cross section of the structure, highlighting the fact that each monolayer is of half unit-cell height. Looking at the top monolayer (shaded in blue) in Figure 1.33b, it can be seen that the top Zn tetrahedra in the monolayer (inside white circles) are oriented in a line along <100> direction, whereas in the underlying monolayer (shaded in pink) they lie in a direction parallel to <010>. Correspondingly, the top P tetrahedra in each monolayer also alternate position. If the rate-determining step in the formation of a half SOD cage (necessary for step advancement) depends on the identity of the

atom in the structure to which it bonds a difference in growth rates as a function of direction can be envisioned.

1.5.5.2 $ZnPO_4$-Faujasite

FAU zincophosphate was synthesized for the first time by Gier and Stucky [161]. ZnPO-FAU belongs to the space group Fd-3, and has a unit cell constant $a = 25.1991$ Å. Its formula is $Na_{67}TMA_{12}Zn(ZnPO_4)\cdot 192H_2O$, where TMA stands for tetramethylammonium. For this investigation, crystals were prepared using the original synthesis at 4 °C [161]. The crystals produced have the typical octahedral morphology [83] and a size of a few microns. The solution used for crystal growth in the experiments was the clear mother-liquor produced as the synthesis takes place and the crystals form. It was taken after just 4 hours of synthesis.

In situ observations of FAU-type ZnPO crystals at low supersaturation conditions showed a "birth and spread" growth mechanism (Figure 1.34). The shape of the 2D nuclei formed is triangular, in accordance with previous *ex situ* observations [147]. At high supersaturation conditions, growth takes place by the advancement of macrosteps with a height of tenths of nanometers.

1.5.6 Metal Organic Frameworks

Nanoporous MOF crystals have bonding halfway between that of weak hydrogen bonding in molecular crystals and strong covalent bonding in zeolites. The first *in situ* AFM images of growing nanoporous crystals were reported on an MOF as the conditions for growth are less aggressive for the microscope than for zeolites. Figure 1.35 shows a series of AFM images of the important copper trimesate, $Cu_3(C_9H_3O_6)_2(H_2O)_3$ (HKUST-1) [162], which is a significant crystalline nanoporous MOF [163] built from $Cu_2(H_2O)_2$ units and benzene-1,3,5-tricarboxylate (BTC) groups and used to form a cubic framework with a three-dimensional nanoporous channel system. The crystals exhibit only (111) facets and the sample has been prepared by growing under ambient conditions in an oriented manner on gold substrates functionalized with self-assembled monolayers

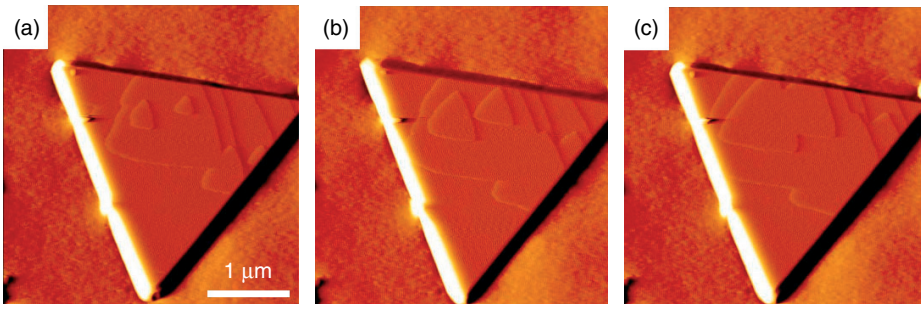

Figure 1.34 Sequence of AFM deflection images showing the growth of nuclei in a ZnPO–FAU crystal.

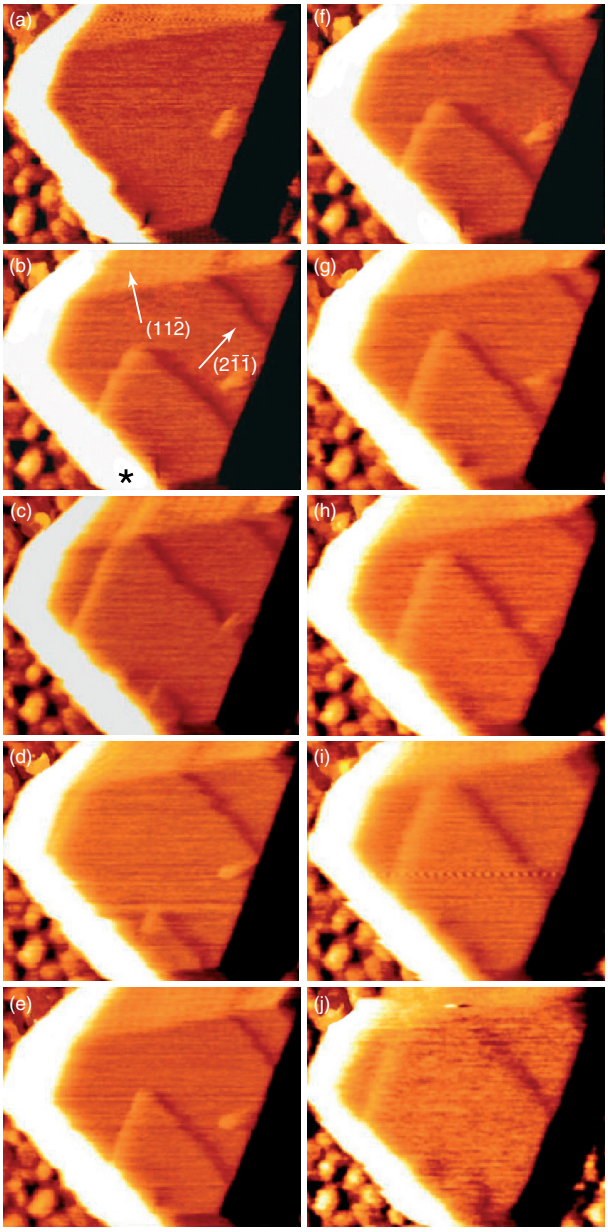

Figure 1.35 Real-time deflection AFM images of the growing {111} facet of a HKUST-1 crystal at (a) 56, (b) 77, (c) 79, (d) 82, (e) 85, (f) 88, (g) 91, (h) 94, (i) 97, (j) 108 minutes, after injection of the growth solution. (Times refer to the end of each scan). Image sizes are $0.763 \times 0.613\ \mu m^2$.

(SAMs) of 16-mercapto-1-hexadecanol [162]. This provides a unique platform for *in situ* AFM studies, since the crystals are firmly anchored by direct attachment to a gold-coated glass substrate, but more importantly, the orientation of the crystals can be tuned by using different functional groups for surface functionalization, such that the growth of the {111} face can be monitored directly.

The crystal growth could be clearly monitored 56 minutes after the injection of the solution used for growth. The image at 56 minutes (Figure 1.35a) reveals an extremely flat and relatively defective-free crystal surface exemplifying the utility of this synthetic protocol to produce high-quality crystal surfaces. In the subsequent images, growth of the surface is seen to proceed by a 2D crystal growth mechanism in which each new crystal layer nucleates at the same point on the crystal surface, indicated by an asterisk in Figure 1.35b. It is likely that a defect at this point on the crystal facet is acting as a nucleation center. Cross-sectional analyses of height images at each time during the growth reveals that the vast majority of growth steps have heights of 1.5 ± 0.1 nm corresponding to the 1.5 nm d_{111} crystal spacing of the HKUST-1 structure, but also half-step d_{222} crystal spacings are observed. Interestingly, the triangular terraces exhibit a linear growth until the apex of the terrace reaches the edge of the crystal. At that point the growth slows considerably, illustrating that the abundance of kink sites near the apex of the triangle is dominant for the propagation of the terrace.

The results suggest that a layer grows by initial attachment of BTC and copper species onto a stably terminated crystal surface to form a small volume of a d'_{222} step with metastable termination. The attachment of additional reagent to the crystal occurs more rapidly at this newly created metastable termination, creating a new d_{111} step with a stable terminated surface.

1.6 Conclusions and Outlook

By applying a number of novel techniques to the problem of crystal growth in nanoporous materials, it is now possible to understand the mechanism at the molecular scale. In particular, the advent of AFM has opened a new window on the subject. Crystals are observed to grow by birth-and-spread mechanism as well as by spiral growth. The effects of supersaturation, temperature, chemical speciation, and structure are becoming apparent at this fundamental scale. It can be hoped that in the near future it should be possible to control crystal shape and habit, defects, and intergrowths through careful control of these growth parameters.

In particular, it can be expected that scanning probe microscopies will develop apace. Most AFMs operate at 1 atm pressure with modest variations of temperature under solution conditions. Hydrothermal AFM has been realized to operate at $P =$ 10 bar and $T = 150^{\circ}$C [164], however, current designs do not permit the location of micron-sized crystals via optical microscopy techniques, and consequently some technique is required to be developed in order to realize this goal. Nevertheless,

we can expect such breakthroughs in the near future that will extend the range of applicability of AFM to more zeolite systems.

In AFM, the cantilever deflection is determined optically using a laser light source that is reflected off the back of the cantilever surface. For crystal growth measurements this poses many difficult choices. The most obvious is that in a solution it is imperative that there is no turbidity present. The solution may be colored but should not contain any particulates that scatter light. Many crystallizations operate in a chemistry regime where substantial light scattering may be expected. Also, in order to monitor crystallization on micron-sized crystals, it is essential to combine the AFM with a high-resolution optical microscope in order to locate the cantilever on the desired crystal facet. Modern AFM design goes to some lengths in order to organize the geometry of the AFM/optical microscope tandem arrangement in order to accommodate the laser path of the AFM and the optical path of the optical microscope. These complications can be overcome if it was possible to determine the tip displacement or force by measuring the resistance change of a piezoelectric material on the cantilever. There are a number of groups who are developing such techniques since the first images were recorded by Tortonese *et al*. [165] If it becomes possible to realize nonoptical methods for cantilever detection under crystal growth conditions, this would considerably expand the application of AFM in this field.

Very recently, the first ever video-rate AFM recorded under solution conditions has been reported [166]. This work is based around a resonant scanning system. Topographic information is then obtained by deflection of the cantilever determined optically. Video-rate AFM until this work has been confined to samples in air, but this new development is particularly interesting for the study of crystal growth or dissolution where it is difficult to bracket the kinetics within a typical AFM frame rate.

Finally, there has been considerabe progress recently to improve the lateral resolution of AFM to atomic, or even subatomic resolution [167]. Applied to the problem of crystal growth, this might permit the direct observation of template molecules at surfaces.

References

1. Subotic, B. and Bronic, J. (2003) in *Handbook of Zeolite Science and Technology* (eds S.M. Auerbach, K.A. Carrado, and P.K. Dutta), Marcel Dekker, New York, p. 1184.
2. Anderson, M.W., Terasaki, O., Ohsuna, T., Philippou, A., Mackay, S.P., Ferreira, A., Rocha, J., and Lidin, S. (1994) *Nature*, **367**, 347–351.
3. Newsam, J.M., Treacy, M.M.J., Koetsier, W.T., and De Gruyter, C.B. (1988) *Proc. R. Soc. London Ser. A: Math. Phys. Eng. Sci.*, **420**, 375–405.
4. Kashchiev, D. (2000) *Nucleation: Basic Theory with Applications*, Butterworth-Heinemann, Oxford.
5. Mullin, J.W. (2001) *Crystallization*, 4th edn, Butterworth-Heinemann, Oxford.
6. Kashchiev, D. and van Rosmalen, G.M. (2003) *Cryst. Res. Technol.*, **38**, 555–574.
7. Elwell, D. and Scheel, H.J. (1975) *Crystal Growth from High-temperature Solutions*, Academic Press, New York.
8. Lasaga, A.C. (1998) *Kinetic Theory in the Earth Sciences*, Princeton University Press, Princeton, p. 811.

9. Kossel, W. (1934) *Annal. Phys.*, **21**, 457–480.
10. Ohara, M. and Reid, R.C. (1973) *Modeling Crystal Growth Rates from Solution*, Prentice-Hall International Series in the Physical and Chemical Engineering Sciences, Prentice-Hall, p. 272.
11. Volmer, M. and Schultz, W. (1931) *Z. Phys. Chem.*, **156**, 1–22.
12. Frank, F.C. (1949) *Discuss. Faraday Soc.*, **5**, 48–54.
13. Burton, W.K., Cabrera, N., and Frank, F.C. (1951) *Philos. Trans. R. Soc. London*, **A243**, 299–358.
14. van Enckevort, W.J.P. and Bennema, P. (2004) *Acta Crystallogr., Sect. A*, **60**, 532–541.
15. Pina, C.M., Becker, U., Risthaus, P., Bosbach, D., and Putnis, A. (1998) *Nature*, **395**, 483–486.
16. Astier, J.P., Bokern, D., Lapena, L., and Veesler, S. (2001) *J. Cryst. Growth*, **226**, 294–302.
17. Aquilano, D., Veesler, S., Astier, J.P., and Pastero, L. (2003) *J. Cryst. Growth*, **247**, 541–550.
18. van der Hoek, B., van der Eerden, J.P., and Tsukamoto, K. (1982) *J. Cryst. Growth*, **58**, 545–553.
19. Zauner, A.R.A., Aret, E., van Enckevort, W.J.P., Weyher, J.L., Porowski, S., and Schermer, J.J. (2002) *J. Cryst. Growth*, **240**, 14–21.
20. Baronnet, A., Amouric, M., and Chabot, B. (1976) *J. Cryst. Growth*, **32**, 37–59.
21. Barrer, R.M. (ed.) (1982) *Hydrothermal Chemistry of Zeolites*, Academic Press, London, p. 360.
22. Cundy, C.S. and Cox, P.A. (2005) *Microporous Mesoporous Mater.*, **82**, 1–78.
23. Flanigen, E.M. and Patton, R.L. (1978) Silica polymorph 76-726744 4073865, 19760927.
24. Nicolle, M.A., Di Renzo, F., Fajula, F., Espiau, P., and Des Courieres, T. (1993) **1**, 313–320.
25. Mintova, S., Olson, N.H., Valtchev, V., and Bein, T. (1999) *Science*, **283**, 958–960.
26. Mintova, S. and Valtchev, V. (1999) *Stud. Surf. Sci. Catal.*, **125**, 141–148.
27. Walton, R.I. and O'Hare, D. (2001) *J. Phys. Chem. Solids*, **62**, 1469–1479.
28. Yang, H., Walton, R.I., Antonijevic, S., Wimperis, S., and Hannon, A.C. (2004) *J. Phys. Chem. B*, **108**, 8208–8217.
29. Kosanovic, C., Bosnar, S., Subotic, B., Svetlicic, V., Misic, T., Drazic, G., and Havancsak, K. (2008) *Microporous Mesoporous Mater.*, **110**, 177–185.
30. Wakihara, T., Kohara, S., Sankar, G., Saito, S., Sanchez-Sanchez, M., Overweg, A.R., Fan, W., Ogura, M., and Okubo, T. (2006) *Phys. Chem. Chem. Phys.*, **8**, 224–227.
31. Cundy, C.S. and Forrest, J.O. (2004) *Microporous Mesoporous Mater.*, **72**, 67–80.
32. Cundy, C.S. and Cox, P.A. (2003) *Chem. Rev.*, **103**, 663–701.
33. Pope, C.G. (1998) *Microporous Mesoporous Mater.*, **21**, 333–336.
34. Bransom, S.H., Dunning, W.J., and Millard, B. (1949) *Discuss. Faraday Soc* 83–95.
35. Giaya, A. and Thompson, R.W. (2004) *AIChE J.*, **50**, 879–882.
36. Thompson, R.W. and Dyer, A. (1985) *Zeolites*, **5**, 202–210.
37. Gora, L. and Thompson, R.W. (1997) *Zeolites*, **18**, 132–141.
38. Čižmek, A., Subotić, B., Kralj, D., Babić-Ivančić, V., and Tonejc, A. (1997) *Microporous Mesoporous Mater.*, **12**, 267.
39. Brar, T., France, P., and Smirniotis, P.G. (2001) *Ind. Eng. Chem. Res.*, **40**, 1133–1139.
40. Bronic, J. and Subotic, B. (1995) *Microporous Mesoporous Mater.*, **4**, 239–242.
41. Warzywoda, J., Edelman, R.D., and Thompson, R.W. (1991) *Zeolites*, **11**, 318–324.
42. Cundy, C.S., Lowe, B.M., and Sinclair, D.M. (1990) **100**, 189–202.
43. Kajcsos, Z., Kosanovic, C., Bosnar, S., Subotic, B., Major, P., Liszkay, L., Bosnar, D., Lazar, K., Havancsak, H., Luu, A.T., and Thanh, N.D. (2009) *Mater. Sci. Forum*, **607**, 173–176.
44. Erdem-Senatalar, A. and Thompson, R.W. (2005) *J. Colloid Interface Sci.*, **291**, 396–404.

45. Mintova, S., Fieres, B., and Bein, T. (2002) *Stud. Surf. Sci. Catal.*, **142A**, 223–229.
46. Chang, C.D. and Bell, A.T. (1991) *Catal. Lett.*, **8**, 305.
47. Flanigen, E.M., Bennett, J.M., Grose, R.W., Cohen, J.P., Patton, R.L., Kirchner, R.M., and Smith, J.V. (1978) *Nature*, **271**, 512–516.
48. Burkett, S.L. and Davis, M.E. (1995) *Chem. Mater.*, **7**, 920–928.
49. Wakihara, T. and Okubo, T. (2005) *Chem. Lett.*, **34**, 276–281.
50. Zhdanov, S.P. and Samulevich, N.N. (1980) Proceedings of the 5th International Conference on Zeolites, pp. 75–84.
51. Bosnar, S. and Subotic, B. (1999) *Microporous Mesoporous Mater.*, **28**, 483–493.
52. Iwasaki, A., Hirata, M., Kudo, I., Sano, T., Sugawara, S., Ito, M., and Watanabe, M. (1995) *Zeolites*, **15**, 308–314.
53. Cundy, C.S., Henty, M.S., and Plaisted, R.J. (1995) *Zeolites*, **15**, 353–372.
54. Cundy, C.S., Henty, M.S., and Plaisted, R.J. (1995) *Zeolites*, **15**, 400–407.
55. Bosnar, S., Antonic, T., Bronic, J., and Subotic, B. (2004) *Microporous Mesoporous Mater.*, **76**, 157–165.
56. Gora, L., Streletzky, K., Thompson, R.W., and Phillies, G.D.J. (1997) *Zeolites*, **18**, 119–131.
57. Kalipcilar, H. and Culfaz, A. (2000) *Cryst. Res. Technol.*, **35**, 933–942.
58. Schoeman, B.J. (1997) *Progress in Zeolite and Microporous Materials, Parts A-C*, pp. 647–654.
59. Caputo, D., Gennaro, B.D., Liguori, B., Testa, F., Carotenuto, L., and Piccolo, C. (2000) *Mater. Chem. Phys.*, **66**, 120–125.
60. Schoeman, B.J. (1997) *Zeolites*, **18**, 97–105.
61. Cundy, C.S., Lowe, B.M., and Sinclair, D.M. (1993) *Faraday Discuss.*, **95**, 235–252.
62. Schoeman, B.J., Sterte, J., and Otterstedt, J.E. (1994) *Zeolites*, **14**, 568–575.
63. Kacirek, H. and Lechert, H. (1975) *J. Phys. Chem.*, **79**, 1589–1593.
64. Kacirek, H. and Lechert, H. (1976) *J. Phys. Chem.*, **80**, 1291–1296.
65. Anderson, M.W. (2001) *Curr. Opin. Solid State Mater. Sci.*, **5**, 407–415.
66. Anderson, M.W., Ohsuna, T., Sakamoto, Y., Liu, Z., Carlsson, A., and Terasaki, O. (2004) *Chem. Commun.*, 907–916.
67. Anderson, M.W., Agger, J.R., Meza, L.I., Chong, C.B., and Cundy, C.S. (2007) *Faraday Discuss.*, **136**, 143–156.
68. Stevens, S.M., Cubillas, P., Jansson, K., Terasaki, O., Anderson, M.W., Wright, P.A., and Castro, M. (2008) *Chem. Commun (Camb.)*, 3894–3896.
69. Terasaki, O. and Ohsuna, T. (2003) *Top. Catal.*, **24**, 13–18.
70. Slater, B., Ohsuna, T., Liu, Z., and Terasaki, O. (2007) *Faraday Discuss.*, **136**, 125–141.
71. Komiyama, M. and Yashima, T. (1994) *Jpn. J. Appl. Phys.*, **33**, 3761–3763.
72. Komiyama, M., Tsujimichi, K., Oumi, Y., Kubo, M., and Miyamoto, A. (1997) *Appl. Surf. Sci.*, **121-122**, 543–547.
73. Yamamoto, S., Sugiyama, S., Matsuoka, O., Honda, T., Banno, Y., and Nozoye, H. (1998) *Microporous Mesoporous Mater.*, **21**, 1–6.
74. Voltolini, M., Artioli, G., and Moret, M. (2003) *Microporous Mesoporous Mater.*, **61**, 79–84.
75. Yamamoto, S., Matsuoka, O., Sugiyama, S., Honda, T., Banno, Y., and Nozoye, H. (1996) *Chem. Phys. Lett.*, **260**, 208–214.
76. Sugiyama, S., Yamamoto, S., Matsuoka, O., Honda, T., Nozoye, H., Qiu, S., Yu, J., and Terasaki, O. (1997) *Surf. Sci.*, **377**, 140–144.
77. Sugiyama, S., Yamamoto, S., Matsuoka, O., Nozoye, H., Yu, J., Zhu, G., Qiu, S., and Terasaki, I. (1999) *Microporous Mesoporous Mater.*, **28**, 1–7.
78. Wakihara, T., Sugiyama, A., and Okubo, T. (2004) *Microporous Mesoporous Mater.*, **70**, 7–13.
79. Anderson, M.W., Agger, J.R., Hanif, N., and Terasaki, O. (2001) *Microporous Mesoporous Mater.*, **48**, 1–9.
80. Agger, J.R., Hanif, N., and Anderson, M.W. (2001) *Angew. Chem. Int. Ed.*, **40**, 4065–4067.

81. Agger, J.R., Hanif, N., Cundy, C.S., Wade, A.P., Dennison, S., Rawlinson, P.A., and Anderson, M.W. (2003) *J. Am. Chem. Soc.*, **125**, 830–839.
82. Dumrul, S., Bazzana, S., Warzywoda, J., Biederman, R.R., and Sacco, A. Jr. (2002) *Microporous Mesoporous Mater.*, **54**, 79–88.
83. Singh, R., Doolittle, J., George, M.A., and Dutta, P.K. (2002) *Langmuir*, **18**, 8193–8197.
84. Meza, L.I., Agger, J.R., Logar, N.Z., Kaucic, V., and Anderson, M.W. (2003) *Chem. Commun.*, 2300–2301.
85. Warzywoda, J., Yilmaz, B., Miraglia, P.Q., and Sacco, A. Jr. (2004) *Microporous Mesoporous Mater.*, **71**, 177–183.
86. Yamamoto, S., Sugiyama, S., Matsuoka, O., Kohmura, K., Honda, T., Banno, Y., and Nozoye, H. (1996) *J. Phys. Chem.*, **100**, 18474–18482.
87. Meza, L.I., Anderson, M.W., Slater, B., and Agger, J.R. (2008) *Phys. Chem. Chem. Phys.*, **10**, 5066–5076.
88. Anderson, M.W., Agger, J.R., Thornton, J.T., and Forsyth, N. (1996) *Angew. Chem. Int. Ed.*, **35**, 1210–1213.
89. Wakihara, T., Sasaki, Y., Kato, H., Ikuhara, Y., and Okubo, T. (2005) *Phys. Chem. Chem. Phys.*, **7**, 3416–3418.
90. Agger, J.R. and Anderson, M.W. (2002) *Impact of Zeolites and Other Porous Materials on the New Technologies at the Beginning of the New Millennium, Parts A and B*, pp. 93–100.
91. Walker, A.M., Slater, B., Gale, J.D., and Wright, K. (2004) *Nat. Mater.*, **3**, 715–720.
92. Binnig, G., Quate, C.F., and Gerber, C. (1986) *Phys. Rev. Lett.*, **56**, 930–933.
93. Binnig, G., Rohrer, H., Gerber, C., and Weibel, E. (1982) *Phys. Rev. Lett.*, **49**, 57–61.
94. Zhong, Q., Inniss, D., Kjoller, K., and Elings, V.B. (1993) *Surf. Sci.*, **290**, L688–L692.
95. Mate, C.M., McClelland, G.M., Erlandsson, R., and Chiang, S. (1987) *Phys. Rev. Lett.*, **59**, 1942–1945.
96. Szlufarska, I., Chandross, M., and Carpick, R.W. (2008) *J. Phys. D Appl. Phys.*, **41**, 123001.
97. McPherson, A., Malkin, A.J., and Kuznetsov, Y.G. (2000) *Annu. Rev. Biophys. Biomol. Struct.*, **29**, 361–410.
98. Bose, S., Hu, X., and Higgins, S.R. (2008) *Geochim. Cosmochim. Acta*, **72**, 759–770.
99. Higgins, S.R., Boram, L.H., Eggleston, C.M., Coles, B.A., Compton, R.G., and Knauss, K.G. (2002) *J. Phys. Chem. B*, **106**, 6696–6705.
100. Teng, H.H., Dove, P.M., and De Yoreo, J.J. (2000) *Geochim. Cosmochim. Acta*, **64**, 2255–2266.
101. Maiwa, K., Nakamura, H., Kimura, H., and Miyazaki, A. (2006) *J. Cryst. Growth*, **289**, 303–307.
102. Radenovic, N., van Enckevort, W., Kaminski, D., Heijna, M., and Vlieg, E. (2005) *Surf. Sci.*, **599**, 196–206.
103. Moret, M., Campione, M., Caprioli, S., Raimondo, L., Sassella, A., Tavazzi, S., and Aquilano, D. (2007) *J. Phys.*, **61**, 831–835.
104. Richter, A. and Smith, R. (2003) *Cryst. Res. Technol.*, **38**, 250–266.
105. Loiola, A.R., da Silva, L.R.D., Cubillas, P., and Anderson, M.W. (2008) *J. Mater. Chem.*, **18**, 4985–4993.
106. Karwacki, L., Stavitski, E., Kox, M.H.F., Kornatowski, J., and Weckhuysen, B.M. (2008) *Stud. Surf. Sci. Catal.*, **174B**, 757–762.
107. Kox, M.H.F., Stavitski, E., Groen, J.C., Perez-Ramirez, J., Kapteijn, F., and Weckhuysen, B.M. (2008) *Chem. Eur. J.*, **14**, 1718–1725.
108. Harris, R.K., Knight, C.T.G., and Hull, W.E. (1981) *J. Am. Chem. Soc.*, **103**, 1577–1578.
109. Harris, R.K. and Knight, C.T.G. (1983) *J. Chem. Soc. Faraday Trans. 2: Mol. Chem. Phys.*, **79**, 1525–1538.
110. Harris, R.K. and Knight, C.T.G. (1983) *J Chem. Soc. Faraday Trans. 2: Mol. Chem. Phys.*, **79**, 1539–1561.
111. Knight, C.T.G. (1988) *J. Chem. Soc. Dalton Trans. Inorg. Chem.*, 1457–1460.
112. Kinrade, S.D., Knight, C.T.G., Pole, D.L., and Syvitski, R.T. (1998) *Inorg. Chem.*, **37**, 4278–4283.
113. Kinrade, S.D., Donovan, J.C.H., Schach, A.S., and Knight, C.T.G.

(2002) *J. Chem. Soc., Dalton Trans.*, 1250–1252.
114. Knight, C.T.G. and Kinrade, S.D. (2002) *J. Phys. Chem. B*, **106**, 3329–3332.
115. Knight, C.T.G., Wang, J., and Kinrade, S.D. (2006) *Phys. Chem. Chem. Phys.*, **8**, 3099–3103.
116. Knight, C.T.G., Balec, R.J., and Kinrade, S.D. (2007) *Angew. Chem. Int. Ed.*, **46**, 8148–8152.
117. Haouas, M. and Taulelle, F. (2006) *J. Phys. Chem. B*, **110**, 22951.
118. Aerts, A., Follens, L.R.A., Haouas, M., Caremans, T.P., Delsuc, M.-A., Loppinet, B., Vermant, J., Goderis, B., Taulelle, F., Martens, J.A., and Kirschhock, C.E.A. (2007) *Chem. Mater.*, **19**, 3448–3454.
119. Follens, L.R.A., Aerts, A., Haouas, M., Caremans, T.P., Loppinet, B., Goderis, B., Vermant, J., Taulelle, F., Martens, J.A., and Kirschhock, C.E.A. (2008) *Phys. Chem. Chem. Phys.*, **10**, 5574–5583.
120. Serre, C., Corbiere, T., Lorentz, C., Taulelle, F., and Ferey, G. (2002) *Chem. Mater.*, **14**, 4939–4947.
121. Gerardin, C., Haouas, M., Lorentz, C., and Taulelle, F. (2000) *Magn. Reson. Chem.*, **38**, 429–435.
122. Gerardin, C., In, M., Allouche, L., Haouas, M., and Taulelle, F. (1999) *Chem. Mater.*, **11**, 1285–1292.
123. Vistad, O.B., Akporiaye, D.E., Taulelle, F., and Lillerud, K.P. (2003) *Chem. Mater.*, **15**, 1639–1649.
124. Shi, J., Anderson, M.W., and Carr, S.W. (1996) *Chem. Mater.*, **8**, 369–375.
125. Egger, C.C., Anderson, M.W., Tiddy, G.J.T., and Casci, J.L. (2005) *Phys. Chem. Chem. Phys.*, **7**, 1845–1855.
126. Bussian, P., Sobott, F., Brutschy, B., Schrader, W., and Schuth, F. (2000) *Angew. Chem. Int. Ed.*, **39**, 3901–3905.
127. Schuth, F., Bussian, P., Agren, P., Schunk, S., and Linden, M. (2001) *Solid State Sci.*, **3**, 801–808.
128. Schuth, F. (2001) *Curr. Opin. Solid State Mater. Sci.*, **5**, 389–395.
129. Pelster, S.A., Schrader, W., and Schuth, F. (2006) *J. Am. Chem. Soc.*, **128**, 4310–4317.
130. Pelster, S.A., Kalamajka, R., Schrader, W., and Schuth, F. (2007) *Angew. Chem. Int. Ed.*, **46**, 2299–2302.
131. Pelster, S.A., Schueth, F., and Schrader, W. (2007) *Anal. Chem.*, **79**, 6005–6012.
132. Pelster, S.A., Weimann, B., Schaack, B.B., Schrader, W., and Schueth, F. (2007) *Angew. Chem. Int. Ed.*, **46**, 6674–6677.
133. Kumar, S., Wang, Z., Penn, R.L., and Tsapatsis, M. (2008) *J. Am. Chem. Soc.*, **130**, 17284–17286.
134. Piana, S., Reyhani, M., and Gale, J.D. (2005) *Nature*, **438**, 70–73.
135. Piana, S., and Gale, J.D. (2005) *J. Am. Chem. Soc.*, **127**, 1975–1982.
136. Piana, S., and Gale, J.D. (2006) *J. Cryst. Growth*, **294**, 46–52.
137. Boerrigter, S.X.M., Josten, G.P.H., van de Streek, J., Hollander, F.F.A., Los, J., Cuppen, H.M., Bennema, P., and Meekes, H. (2004) *J. Phys. Chem. A*, **108**, 5894–5902.
138. Umemura, A. (2009) PhD thesis, The University of Manchester, Manchester.
139. Anderson, M.W., Meza, L.I., Agger, J.R., Attfield, M.P., Shoaee, M., Chong, C.B., Umemura, A., and Cundy, C.S. (2008) *Turning Points in Solid-State, Materials and Surface Science*, 95–122.
140. Umemura, A., Cubillas, P., Anderson, M.W., and Agger, J.R. (2008) *Stud. Surf. Sci. Catal.*, **174A**, 705–708.
141. Breck, D.W. (1974) *Zeolite Molecular Sieves*, John Wiley & Sons, Ltd, New York.
142. Baerlocher, C., Meier, W.M., and Olson, D.H. (2007) *Atlas of Zeolite Structure Types*, 7th edn, Elsevier, Amsterdam.
143. Charnell, J.F. (1971) *J. Cryst. Growth*, **8**, 291–294.
144. Petranovskii, V., Kiyozumi, Y., Kikuchi, N., Hayamisu, H., Sugi, Y., and Mizukami, F. (1997) *Stud. Surf. Sci. Catal.*, **105A**, 149–156.
145. Gora, L. and Thompson, R.W. (1995) *Zeolites*, **15**, 526–534.
146. Agger, J.R., Pervaiz, N., Cheetham, A.K., and Anderson, M.W. (1998) *J. Am. Chem. Soc.*, **120**, 10754–10759.
147. Wakihara, T. and Okubo, T. (2004) *J. Chem. Eng. Jpn.*, **37**, 669–674.

148. Thompson, R.W. and Huber, M.J. (1982) *J. Cryst. Growth*, **56**, 711–722.

149. Yang, X.B., Albrecht, D., and Caro, E. (2006) *Microporous Mesoporous Mater.*, **90**, 53–61.

150. Meza, L.I., Anderson, M.W., and Agger, J.R. (2007) *Chem. Commun (Camb.)*, 2473–2475.

151. Meza, L.I., Anderson, M.W., Agger, J.R., Cundy, C.S., Chong, C.B., and Plaisted, R.J. (2007) *J. Am. Chem. Soc.*, **129**, 15192–15201.

152. Brent, R. and Anderson, M.W. (2008) *Angew. Chem. Int. Ed.*, **47**, 5327–5330.

153. Castro, M., Garcia, R., Warrender, S.J., Slawin, A.M.Z., Wright, P.A., Cox, P.A., Fecant, A., Mellot-Draznieks, C., and Bats, N. (2007) *Chem. Commun.*, 3470–3472.

154. Cubillas, P., Castro, M., Jelfs, K.E., Lobo, A.J.W., Slater, B., Lewis, D.W., Wright, P.A., Stevens, S.M., and Anderson, M.W. (2009) *Crys. Growth Des.*

155. Paquette, J. and Reeder, R.J. (1995) *Geochim. Cosmochim. Acta*, **59**, 735–749.

156. Lewis, D.W., Willock, D.J., Catlow, C.R.A., Thomas, J.M., and Hutchings, G.J. (1996) *Nature*, **382**, 604–606.

157. Jelfs, K.E., Slater, B., Lewis, D.W., and Willock, D.J. (2007) *Zeolites to Porous MOF Materials*, Vol. 170B, Elsevier B.V., pp. 1685–1692.

158. Nenoff, T.M., Harrison, W.T.A., Gier, T.E., and Stucky, G.D. (1991) *J. Am. Chem. Soc.*, **113**, 378–379.

159. Harrison, W.T.A., Gier, T.E., and Stucky, G.D. (1991) *J. Mater. Chem.*, **1**, 153–154.

160. Nenoff, T.M., Harrison, W.T.A., Gier, T.E., Calabrese, J.C., and Stucky, G.D. (1993) *J. Solid State Chem.*, **107**, 285–295.

161. Gier, T.E., and Stucky, G.D. (1991) *Nature*, **349**, 508–510.

162. Shoaee, M., Agger, J.R., Anderson, M.W., and Attfield, M.P. (2008) *Cryst EngComm*, **10**, 646–648.

163. Chui, S.S.Y., Lo, S.M.F., Charmant, J.P.H., Orpen, A.G., and Williams, I.D. (1999) *Science*, **283**, 1148–1150.

164. Higgins, S.R., Eggleston, C.M., Knauss, K.G., and Boro, C.O. (1998) *Rev. Sci. Instrum.*, **69**, 2994–2998.

165. Tortonese, M., Barrett, R.C., and Quate, C.F. (1993) *Appl. Phys. Lett.*, **62**, 834–836.

166. Picco, L.M., Bozec, L., Ulcinas, A., Engledew, D.J., Antognozzi, M., Horton, M.A., and Miles, M.J. (2007) *Nanotechnology*, **18**, 044030-1–044030-4.

167. Giessibl, F.J. and Quate, C.F. (2006) *Phys. Today*, **59**, 44–50.